Impact of secondary coatings on the dissolution rate of K-feldspar: A combined experimental and modeling study

Marion Pollet-Villard, Arnaud Bouissonnié, Gerhard Schäfer, Philippe Ackerer, Bertrand Fritz, Martiane Cabié, Damien Daval

Impact of secondary coatings on the dissolution rate of K-feldspar: A combined experimental and modeling study

Marion Pollet-Villard[1], Arnaud Bouissonnié[1,2], Gerhard Schäfer[1], Philippe Ackerer[1], Bertrand Fritz[1], Martiane Cabié[3], Damien Daval[1,4,*]

[1] Université de Strasbourg / CNRS / ENGEES – Institut Terre et Environnement de Strasbourg, UMR 7063, Strasbourg, France

[2] Institute for Carbon Management, University of California, Los Angeles, CA, United States

[3] Aix Marseille Université, CNRS, Centrale Marseille, FSCM, CP2M, Marseille, France

[4] Université Grenoble Alpes, Université Savoie Mont Blanc, CNRS, IRD, Université G. Eiffel, ISTerre, Grenoble, France

* Corresponding author: damien.daval@univ-grenoble-alpes.fr

Keywords: K-feldspar; hydrothermal alteration; dissolution-reprecipitation experiments; geothermal reservoir

Submitted to *Geothermics*

Abstract

Heat transfer fluid mining represents a thermodynamic perturbation for geothermal reservoirs: The pumping of hot water coupled with the re-injection of colder water at depth favors the dissolution of some rock-forming minerals of the deep reservoir (e.g. feldspars), while promoting the precipitation of secondary phases, resulting in a possible change in the permeability and porosity of the reservoir. Such an impact is even greater when one considers the acid stimulations aimed at increasing the injectivity of the geothermal system. In that respect, no consensus exists in the literature regarding the impact of secondary phases on the dissolution rate of primary phases and therefore, on the sustained modification of pore structure. The present study aimed at shedding new light on these questions. Hydrothermal experiments of K-feldspar alteration were conducted at conditions relevant for the geothermal reservoir of Soultz-sous-Forêts (T = 180 °C, acidic pH domain). Measurements of cation release rates were combined with characterizations of secondary coatings (mineralogy, extent of coverage, thickness and porosity) to determine the reactivity of submillimeter K-feldspar powders with and without secondary precipitates. The formation of µm-thick boehmite coatings on K-feldspar grains was found to result in a modest decrease in its reactivity, which might be better explained by the presence of dissolved Al in the bulk solution. This result was independently confirmed by reactive transport simulations, which revealed that the impact of secondary coatings may become significant only when their thickness exceeds a few tens of microns, or if the dissolution rate of the primary phase is significantly greater (10^6 times) than that of orthoclase. Taken together, this study offers new constraints on the intricate interplay between dissolution and precipitation reactions, of prime importance for modeling more accurately the impact of mass transfer and porosity generation resulting from fluid circulation in geothermal reservoirs.

1. Introduction

Enhanced geothermal systems (EGS), which generate geothermal electricity by circulating water in subsurface environments with a positive thermal anomaly, are among the strategies that are frequently invoked to contribute to the decarbonization of energy sources and reduce greenhouse gas emissions. 'Hot Dry Rock' (HDR) projects emerged in the middle of the 1980s, aiming to circulate heat-bearing fluids in closed loops to harness the heat stored in deep rocks through fracture networks developed in the rock by fracking. In parallel, several groups over the world explored complementary strategies, such as those consisting in taking advantage of the geothermal potential that could be offered by naturally fractured deep crystalline rocks that may maintain deep natural convective loops. These circulation paths could be used for heat transfer fluid mining without additional fracking. In that respect, the Soultz-sous-Forêts geothermal power plant located in the Upper Rhine Graben, 50 km north of Strasbourg, represented one of such pioneering sites in France that has been selected as it exhibits a strong thermal anomaly, extensively studied since the 1920s and oil field research in that area (Munck et al., 1979; Gérard et al., 1984). The subsurface at this site is a natural deep hydrothermal system with a geothermal gradient noticeably higher than normal in the first km of the sedimentary cover (~100 °C/ km) and natural brine circulation in the underlying fractured granite, which is responsible for a reduced geothermal gradient (30 °C/km) between 1 and 3.5 km. The Soultz-sous-Forêts geothermal project was initiated by a French-German team in 1986, and has been in operation for almost 40 years, supplying electricity since 2008 (a summary of the history of the project can be found in e.g., Genter et al., 2010).

From a geochemical standpoint, the pumping of hot water coupled with the re-injection of colder water at depth favors the dissolution of some rock-forming minerals of the deep reservoir (e.g. feldspars), while promoting the precipitation of secondary phases (Fritz et al.,

2010; Ngo et al., 2016). The relative intensities of primary mineral leaching and secondary phase formation may affect porosity and permeability of the reservoir, thereby influencing its hydraulic performance. Such changes in mineral composition and reservoir permeability / porosity are among the most important parameters when acid stimulations, aimed at increasing the productivity and injectivity of a given geothermal system, are considered (e.g. Lucas et al., 2020). Therefore, predicting the fate of fluid injection in geological reservoirs represents a critical issue for evaluating the modification of reservoir permeability / porosity resulting from fluid-rock interactions in general (Cui et al., 2021a, b), and the efficiency of EGS in particular (Alt-Epping et al., 2013a; Alt-Epping et al., 2013b; Griffiths et al., 2016; Lucas et al., 2020; Vital et al., 2020). However, the predictive ability of reactive transport models is frequently questioned. Indeed, the kinetics of water-rock interactions are rarely successfully reproduced without the use of fitting parameters, most often aimed at refining the "effective surface area" of minerals, whose value remains somewhat arbitrarily fixed in modeling exercises, and supposed to be related to the proportion of the surface of primary minerals that is not covered by secondary phases (e.g. Montes-H et al., 2005; Maher et al., 2009; Aradóttir et al., 2012).

This fundamental issue has given rise to a wealth of experimental and theoretical work aimed at investigating the feedback effects between coupled dissolution and precipitation reactions, some of the main results of which are briefly reviewed below. On the one hand, coupled dissolution-precipitation reactions were demonstrated to act as an autocatalytic system, where the consumption by secondary precipitates of the released ions maintains conditions of undersaturation with respect to the primary phases, thereby sustaining a high dissolution flux, resulting in an equally high precipitation rate of secondary phases (e.g. Putnis, 2002; Frugier et al., 2008; Putnis, 2009 and references therein). On the other hand, the formation of secondary phases has also long been suspected to potentially result in so-called

98 “armoring” or “passivating” effects, preventing the transport of reactants between the bulk
99 fluid and the surface of the dissolving primary phases (Luce et al., 1972; Velbel, 1993).
100 Several parameters were identified as crucial in predicting the passivating ability of a given
101 coating, including (i) the molar volume ratio of product to reactant (with ratio > 1 possibly
102 resulting in passivation of the primary phrases Velbel, 1993); (ii) the potential
103 crystallographic relationships between primary and secondary phases (with epitaxial growth
104 favoring passivation; e.g. Cubillas et al., 2005); or (3) if the coating is a silica gel, its potential
105 evolution from a porous to a denser and less permeable structure due to various aging
106 mechanisms (Gin et al., 2001; Cailleteau et al., 2008; Gin et al., 2015; Saldi et al., 2015;
107 Daval et al., 2017; Daval et al., 2018; Fournier et al., 2019).
108 Overall, previous experimental work suggested that secondary phases can have opposite
109 impacts on the dissolution of the parent phases, and the extent of coverage resulting from
110 mineral precipitation has often been used in modeling exercises as a fitting parameter to
111 decrease accordingly the proportion of the surface area of the mineral that actually contributes
112 to the dissolution flux. To shed new light on these questions, the present study was designed
113 to investigate the impact of secondary coatings on the reactivity of K-feldspar, one of the
114 main rock-forming minerals in granitic geothermal reservoirs, such as the one at the Soultz-
115 sous-Forêts site. At this site, K-feldspar represents 23.6 vol% of the fresh granite
116 composition, other major phases including plagioclase (42.5 vol%), quartz (24.2 vol%), and
117 biotite (4.2 vol%) (Fritz et al., 2010). The experiments were conducted under conditions
118 relevant for this specific site of interest, in acidic solutions ($T = 180$ °C; $2 < pH < 4$). The
119 reasons for targeting these pH conditions are two-fold: first, they are well suited to simulating
120 the impact of an acid stimulation of the reservoir, as the HCl concentration of the stimulating
121 fluid can be as high as 0.45% (pH ~ 1) (Lucas et al., 2020) while the pH of granitic reservoirs
122 is generally slightly acidic (e.g., close to 4.8 in the case of Soultz-sous-Forêts; Fritz et al.,

2010). Secondly, from an experimental standpoint, running experiments in the acid pH range makes it possible to take advantage of the low solubility of Al at high temperature (< 10^{-5} M for 2 < pH < 7 at 180 °C) to develop secondary coatings on timescales of days to weeks. Although investigating the impact of barite on K-feldspar dissolution could have been considered even more relevant in the case of Soultz-sous-Forêts as barite represents one of the most abundant scaling phases (e.g., Griffiths et al., 2016 and references therein), the massive precipitation of barite remains out of reach experimentally, as it results from the long-term release of trace amounts of barium contained in K-feldspar (e.g., Pauwels et al., 1993; Azaroual and Fouillac, 1997). Therefore, we purposely decided to focus on studying the impact of major Al-rich secondary phases resulting from the dissolution of a primary rock-forming mineral to specifically investigate a model coupled interfacial dissolution-reprecipitation system (i.e., where secondary phases grow directly at the contact surface with the primary dissolving phase) because of its broad relevance for a wide range of geological processes (Ruiz-Agudo et al., 2014). In addition, as the acid stimulation on site may eventually drive K-felspar dissolution and additional Ba release in the fluid, this enhanced dissolution may compete with barite removal targeted by the acid stimulation on the longer terms. As detailed below, the use of reactive transport modeling enabled us to unravel the contribution of secondary coatings to the modest decline in K-feldspar reactivity observed experimentally and to provide guidelines for anticipating the conditions under which secondary coatings may have a significant impact on the reactivity of primary phases.

2. Materials and methods

2.1 Sample characterization and preparation of K-feldspar powders

Preliminary experiments were first conducted with K-feldspar originating from the Soultz-sous-Forêts site. However, the phenocrysts isolated from the granitic reservoir contain

148 several wt.% of accessory minerals and are perthitic in nature, resulting in the preferential
149 dissolution of the albitic domains, which made it impossible to properly isolate the impact of
150 secondary phases on K-feldspar reactivity following the approach described below. As a
151 consequence, the selected starting material was a natural K-feldspar (orthoclase) crystal
152 coming from Afghanistan, which we already described in some of our previous work (Pollet-
153 Villard et al., 2016a; Pollet-Villard et al., 2016b). In brief, no minor phases were detected
154 with scanning electron microscopy (SEM) or X-ray diffraction (XRD), bearing in mind that
155 the detection limit of the apparatus we used is close to 1 wt.%. The chemical composition of
156 the sample ($K_{0.75}Na_{0.22}Fe_{0.01}Al_{0.98}Si_{3.02}O_8$) was determined by Inductively Coupled Plasma
157 Atomic Emission Spectroscopy (ICP-AES; THERMA® ICAP 6000 Series) after a standard
158 alkaline digestion. Dissolution experiments were carried out on orthoclase powders. Powders
159 were obtained after crushing centimeter-sized orthoclase single crystals with a hydraulic press
160 and sieving to recover the 800-1000 µm-sized fraction. Fine particles were removed from this
161 powder by five successive water baths followed by several ultrasonic cleaning in ethanol until
162 the discarded supernatant became clear. The resulting orthoclase powder was then dried at 40
163 °C during two hours. After cleaning cycles, a part of the powder was analyzed with a Tescan®
164 VEGA II SEM to control that the powder was free of fine particles (Fig. S1). The specific
165 surface area of the powder, measured with 7-points Kr BET, was 0.012 $m^2.g^{-1}$.

166 **2.2 Aqueous alteration experiment**

167 Powders were reacted in a synthetic acidic solution in a Parr® mixed-flow reactor (see
168 Fig. S1b and Hellmann et al., 1997 for more details) at 180 °C and 50 bars for durations
169 ranging from one to three weeks. Inlet solutions were made with ultrapure deionized water
170 (18.2 MΩ.cm) and analytical grade Na_2SiO_3, LiCl and $AlCl_3$ powders and HCl. The pH was
171 adjusted with the concentration of HCl in the solution. No pH buffer was used in solution

because buffers can influence the dissolution rate of silicates (e.g. Golubev and Pokrovsky, 2006).

Before each experiment, the system was cleaned in a 0.1 M HCl bath for several hours and was subjected to a circulation (at a flow rate v = 1 mL.min^{-1}) of 0.01 M HCl solution for 2 hours. Then, the inlet solution (used to carry out alteration experiments) was circulated in the reactor (without powder) for at least three days, at 180 °C, until the concentrations of K, Al and Si were below the detection limit. After this cleaning procedure, powders were introduced in the reactor to start the alteration experiments. Each experiment was performed at constant temperature (180 °C), pressure (50 bars), flow rate and inlet solution composition (Tables 1 and 2).

Table 1. Chemical conditions of experiments aimed at forming secondary coatings on orthoclase grains (MPA experiments).

	Duration	Flow rate	Mass	Inlet concentrations (mol.L^{-1})					
	(days)	(mL.min^{-1})	(g)	Si	Al	Na	K	Cl	Li
MPA1	9	0.1	0.1957	-	-	-	-	2.00E-2	1.00E-2
MPA2	9	0.1	0.4037	-	-	-	-	1.10E-2	1.00E-2
MPA3	17	0.1	0.4002	-	-	-	-	2.00E-2	1.00E-2
MPA4	9	0.1	0.4042	-	-	-	-	1.0E-4	-
MPA5	19	0.1	0.4118	-	-	-	-	5.65E-5	-
MPA6	12	0.1	0.4100	2.06E-4	2.00E-4	4.32E-4	-	7.00E-7	-
MPA7	9	0.13	0.4976	2.06E-4	2.00E-4	4.55E-4	-	1.60E-3	-
MPA8	11	0.15	0.4186	1.21E-4	1.00E-4	2.22E-4	-	1.03E-2	-
MPA9	16	0.1	0.4016	-	-	-	-	1.00E-2	-

	Outlet concentrations (mol.L^{-1})						pH	Ionic strength	ΔGr
	Si	Al	Na	K	Cl	Li		(mol.L^{-1})	(kJ.mol^{-1})
MPA1	3.09E-4	6.42E-5	1.78E-5	7.64E-5	2.00E-2	1.00E-2	2.1	2.00E-2	-72
MPA2	3.29E-4	2.63E-7	1.93E-5	8.52E-5	1.1E-2	1.00E-2	3.1	1.1E-2	-67
MPA3	5.38E-4	3.40E-5	3.00E-5	1.32E-4	2.00E-2	1.00E-2	2.1	2.00E-2	-66
MPA4	1.29E-4	1.50E-7	7.90E-6	3.80E-5	1.00E-4	-	4.3	1.00E-4	-70
MPA5	9.31E-5	2.50E-6	1.05E-5	2.60E-8	5.65E-5	-	4.7	5.70E-5	-65
MPA6	5.30E-4	9.80E-6	5.10E-4	8.30E-5	7.00E-4	-	3.8	7.00E-4	-49
MPA7	5.80E-4	9.50E-7	4.8E-4	1.00E-4	1.6E-3	-	3.0	1.60E-3	-48
MPA8	5.85E-4	3.50E-4	2.47E-4	1.34E-4	1.03E-2	-	2.1	1.00E-2	-64
MPA9	5.60E-4	4.14E-5	3.19E-5	1.51E-4	1.00E-2	-	2.1	1.00E-1	-63

The first four columns indicate the name of the experiments, their duration (days), the fluid flow rate and the initial powder mass. The following columns list the concentrations of the elements in the inlet and outlet solutions, determined by ICP-AES analysis. The last three columns show the *in situ* pH, the ionic strength and the Gibbs free energy with respect to orthoclase dissolution reaction, calculated using CHESS software.

During experiments, the outlet fluid was sampled daily. The composition of the outlet fluid reached a steady-state after a few days of alteration, which correspond, at least, to three fluid residence times (defined as the reactor volume divided by the flow rate). Concentrations of Si, Al and K in the inlet and the outlet solutions were measured by ICP-AES and are listed in Tables 1 and 2. Outlet fluid compositions correspond to the mean aqueous concentrations at steady-state conditions. The analytical uncertainties in the ICP-AES measurements, based on repeated analyses of standard solutions and blanks, were estimated to be better than ±10% (typically 6–7%). The CHESS code (van der Lee and De Windt, 2002), which is a computer model for speciation, batch-reaction, and inverse geochemical calculations, was used to determine the *in situ* pH, the ionic strength and saturation indices with respect to orthoclase and secondary phases (Table 3).

Table 2. Chemical conditions of dissolution experiments on fresh orthoclase powder.

	Duration	Flow rate	Powder mass	Steady-state outlet concentrations (mol.L^{-1})					pH	Ionic strength
	(days)	(mL.min−1)	(g)	Si	Al	Na	K	Cl		(mol.L−1)
MDA3	5	0.5	0.0524	2.90E-05	9.20E-06	1.99E-05	7.80E-06	1.00E-02	2.1	1.00E-02
MDA4	6	0.36	0.0522	3.59E-05	1.10E-05	2,50E-6E	9.50E-06	1.00E-02	2.1	1.00E-02
MDA5	8	0.6	0.0526	2.35E-05	7.90E-06	1.45E-06	5.80E-06	1.00E-02	2.1	1.00E-02
MDA6	7	0.66	0.0519	1.60E-05	4.95E-06	1.40E-06	3.65E-06	1.00E-02	2.1	1.00E-02
MDA8	14	0.66	0.0504	1.85E-05	5.98E-06	7.74E-07	4.69E-06	1.26E-02	2.0	1.25E-02

The first four columns indicate the name of the experiments, their duration, the fluid flow rate and the initial mass of powder. The following columns list the concentrations of the elements in the solution sampled downstream of the reactor. These concentrations were determined by ICP-AES analysis. The last two columns show the *in situ* pH and the ionic strength.

Table 3. Thermodynamic status of aqueous solutions in the MDAf experiments.

	ΔGr(K-spar)	log(Q/K)				
	(kJ.mol^{-1})	SiO_2(am)	Gibbsite	Boehmite	Corundum	Diaspore
MDA3	-144	-2.658	-0.904	-0.397	-0.132	-0.189
MDA4	-110	-2.546	-0.828	-0.321	0.021	-0.113
MDA5	-118	-2.749	-0.973	-0.465	-0.269	-0.258
MDA6	-126	-2.916	-1.177	-0.669	-0.676	-0.462
MDA8	-126	-2.853	-1.331	-0.823	-0.984	-0.616

The Gibbs free energy with respect to orthoclase dissolution reaction is reported first. The saturation indices (log(Q/K)) for secondary phases likely to precipitate are reported next. These calculations were run using CHESS software.

The experimental strategy is depicted in Fig. 1. In brief, five different series of experiments were performed:

(1) Dissolution experiments at pH 2 (hereafter referred to as MDAf) in solutions undersaturated with respect to any secondary phase. These experiments aimed at providing an accurate baseline of the reactivity of fresh orthoclase powders devoid of secondary coatings, at far-from-equilibrium conditions;

(2) Coupled precipitation/dissolution reactions (hereafter referred to as MPA-pH2), where orthoclase dissolution rates were measured at pH 2 during boehmite precipitation. These experiments aimed at deciphering the impact of precipitated boehmite on orthoclase dissolution rate;

(3) Coupled precipitation/dissolution reactions carried out at pH > 2 (hereafter: MPA-pH>2), where the increase in pH possibly resulted either in the thickening of the secondary coating coverage on orthoclase grains, a modification of their texture or a modification of the nature of the precipitated minerals. The final coated orthoclase powders were then recovered to be used as starting materials for the series MDAc described below;

(4) Dissolution experiments at pH 2 of the final powders recovered at the end of MPA-pH>2 and covered with secondary coatings (hereafter referred to as MDAc). These experiments aimed at estimating the impact of the coatings synthesized in the series MPA-pH>2 on the dissolution rate of orthoclase. Note that because the solubility of Al-bearing phases decreases with temperature, the powders were recovered at warm (40 °C; MPA1-MPA5) to hot (95 °C; MPA6-MPA9) temperatures to prevent dissolution of the coatings during the quench phase;

(5) Finally, a last experiment (hereafter referred to as: MPDA) was realized following two steps: in the first step, a fresh orthoclase powder was altered in a pH 4 solution enriched in Al(aq) in order to precipitate coatings of secondary Al-bearing minerals. After 11 days, the inlet solution was replaced with a pH 2 solution, and the dissolution rate of orthoclase was monitored through the measurements of aqueous K and Si. This experiment was designed to circumvent the potential damages of the coatings covering orthoclase at the end of the MPA-pH>2 series: actually, the decrease in pressure and temperature might have resulted in a modification of the texture of the secondary coatings. Therefore, experiment MPDA improved upon such potential shortcomings.

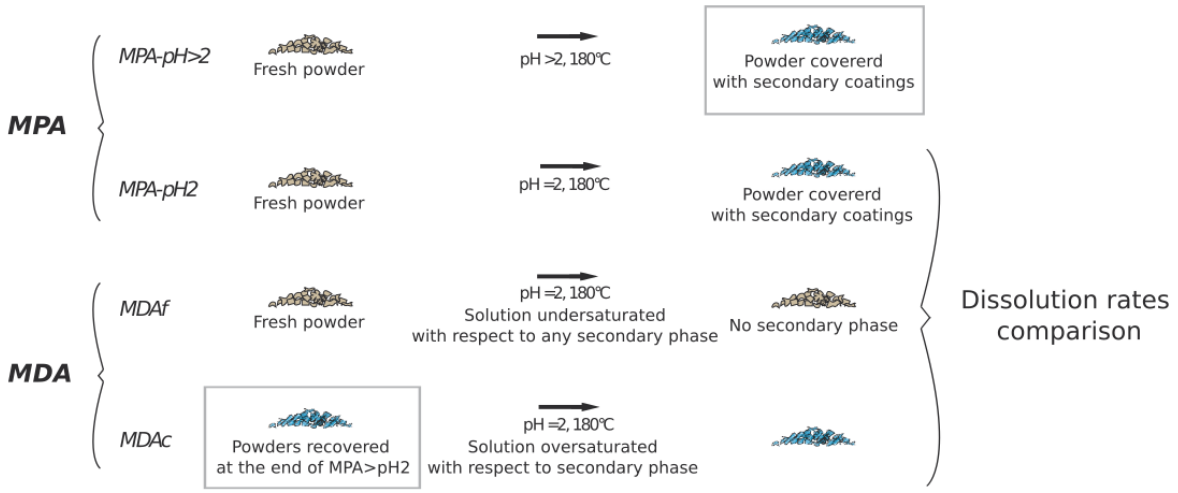

Fig. 1. Schematic of the experimental strategy followed in the present study. See text for details.

For each experiment, orthoclase dissolution rates were calculated from the steady-state outlet concentrations of K and Si at the end of each experiment, following the equation (see e.g. Daval et al., 2010 for details):

$$r_i = \frac{v.[i]}{\eta_i.SSA.m_0} \quad (1)$$

where v is the flow rate ($l.s^{-1}$), $[i]$ is the outlet concentration of a solute i ($mol.l^{-1}$), η_i is the stoichiometric coefficient of element i in the mineral, SSA is the specific surface area ($m^2.g^{-1}$), and m_0 is the starting mass of orthoclase (g), such that r_i is expressed in $mol.m^{-2}.s^{-1}$.

253 **2.3 Coating characterizations**

254 At the end of each experiment, the reacted orthoclase powders were rinsed with ethanol
255 and dried at 35°C during a few minutes to perform SEM and XRD analyses.

256 *2.3.1 XRD characterizations*

257 The mineralogical composition of the secondary coatings was characterized by X-ray
258 diffraction. Samples were analyzed with a diffractometer equipped with a Cu anticathode, at
259 40 kV and 30 mA (Bruker D5000). Scans were taken for 2θ ranging from 3° to 65° with
260 0.03°/step, 25 s /step).

261 *2.3.2 SEM characterizations and focused ion beam milling*

262 SEM analyses of the final powders were conducted to estimate the chemical composition
263 of the secondary coatings (using energy dispersive X-ray spectroscopy (EDXS), Edax
264 PEGASUS) and the proportion of the surface of orthoclase that was covered by secondary
265 coatings in each experiment. The powders were carbon-coated and analyzed with backscatter
266 electron (BSE), which is sensitive to the chemical composition of the surface. BSE images
267 were then processed by gray thresholding (Fig. S2) using the ImageJ software (Abràmoff et
268 al., 2004; Schneider et al., 2012) in order to calculate the proportion of orthoclase surface area
269 coated with secondary phases. Measurements were carried out on a dozen of grains for each
270 experiment. A part of the altered powders was also embedded into epoxy resin and polished
271 through a multistep abrasive sequence using diamond suspensions of decreasing grain sizes
272 and soft polishing cloths. Resulting samples were used to measure the thickness of secondary
273 coatings with SEM analysis (Fig. S3).

274 Samples embedded in resin and polished were also used to estimate the porosity of
275 coating. Ultrathin cross sections were milled by focused ion beam (FIB) through the coating
276 (Fig. S4) using a HELIOS® 600 NANOLAB dual beam equipment operated at CP2M,
277 Marseille, France. FIB Ga^+ ion milling was carried out at an ion beam voltage of 30 kV and

beam current of 0.9 nA. High resolution backscatter electron images were acquired with an in-lens detector at a beam voltage of 2 kV and beam current of 0.17 nA. Multiple successive sections were realized throughout the coatings following this method. The corresponding SEM images were processed by grey thresholding using ImageJ (Fig. S4). This protocol was followed to estimate the porosity of the coatings formed on the grains from experiments MPA3 and MPA6.

2.4 Numerical reactive transport model

As emphasized from a theoretical standpoint by e.g. Emmanuel, 2022 or experimentally by Ruiz-Agudo et al., 2016, secondary coatings formed on the surface of primary minerals may act as a diffusion barrier, limiting the transport of solutes that promote dissolution, such as protons. To test this hypothesis, a simple 1D reactive transport model was developed and run using the physical properties of the coatings determined experimentally.

Let us consider the transport of H^+ ions in a porous medium. The transport equation in the direction x can be written using the classical diffusion equation:

$$\varphi \frac{\partial C}{\partial t} = \frac{\partial}{\partial x}\left(D \frac{\partial C}{\partial x}\right) \quad (2)$$

where C (mol.m^{-3}) denotes the proton concentration, D (m^{2}s^{-1}) represents the effective diffusion coefficient and φ is the porosity of the medium. The mathematical formulation of the effective diffusion coefficient can be given by (e.g., Archie, 1942):

$$D = D_0 \varphi^m \quad (3)$$

where D_0 (m^{2}s^{-1}) is the water self-diffusion coefficient and m the cementation factor of the medium.

The finite volume method was used to solve Eq. (2). The study area is a 1D domain discretized into N equally spaced cells, where k represents the cell center, k-1/2 is the upstream cell edge and k+1/2 is the downstream cell edge. The parameters C and φ are

defined at the center of the cell, whereas D is defined at the cell edges. The integration of the transport equation (Eq. 2) is described in detail in the Appendix.

Initially, the H^+ concentration in the porosity of the coating is considered negligible compared to the concentration in the solution upstream of the coating (i.e., $C(t=0) = 0$).

At $x = 0$, the concentration (C_0) is fixed at a constant value imposed by the pH of the bulk fluid. At the boundary between the coating and orthoclase, the concentration depends on a sink term (P) due to the H^+ consumption rate by the orthoclase dissolution reaction. Given that the dissolution rate of orthoclase varies as the square root of proton concentration in the aqueous medium (Palandri and Kharaka, 2004), the sink term can be written following:

$$P = \frac{4r_0}{\varphi_N \Delta x}\sqrt{\frac{C_N^t}{C_0}} \quad (4)$$

In equation (5), r_0 (mol.m^{-2}.s^{-1}) is the orthoclase dissolution rate in a solution containing a H^+ concentration equal to C_0 , C_N^t and φ_N correspond to the H^+ concentration in cell N at time t and porosity of cell N, respectively, and Δx is the size of the cell. The factor 4 results from the stoichiometry of the dissolution reaction, as 4 moles of H^+ ions are consumed per mole of orthoclase. The sink term is integrated in the downstream boundary condition of the numerical transport model as shown in the matrix form of Eq. A6 (see Appendix). In this simple model, we do not consider the possible evolution of the speciation in the fluid, nor the impact of ΔG_r, as this parameter does not play a significant role in the acidic pH domain (see Section 4.1).

3. Experimental results

3.1 Experiments conducted at pH 2 on fresh powders in undersaturated conditions with respect to secondary phases (experiments MDAf)

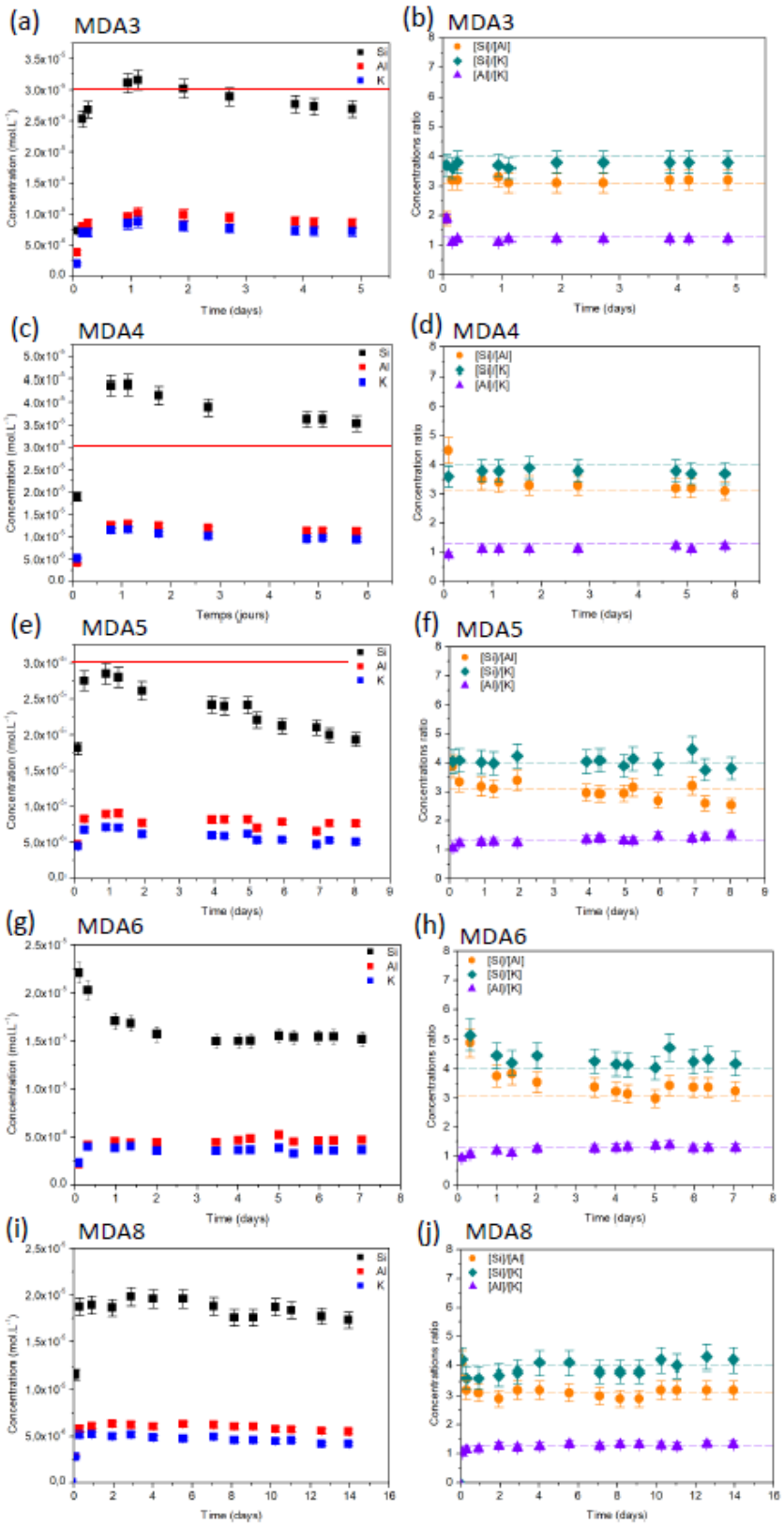

Fig. 2. Time-resolved fluid analyses of MDAf experiments. (a, c, e, g, i) Time-resolved concentrations of released elements (outlet concentration subtracted from inlet concentration). The red lines indicate boehmite solubility. (b, d, f, h, j) ratios of these concentrations. The dashed lines represent the theoretical values of these ratios for stoichiometric dissolution. The MDAf experiments were carried out at pH 2 and under conditions of undersaturation with respect to Al-bearing secondary phases.

The concentrations of elements released during orthoclase dissolution (i.e., the difference between the outlet concentrations and the concentration measured in the blanks) are shown in Fig. 2, corresponding to experiments MDA3, MDA4, MDA5, MDA6 and MDA8. From these data, the [Si]/[Al] and [Si]/[K] ratios were calculated to check whether the stoichiometry of orthoclase was respected (Fig. 2b). Note that the uncertainties in the concentration measurements are between 5% and 10%.

Steady-state conditions were reached for all experiments, with the possible exception of MDA5, where the Si concentration appeared to decrease slightly over time (Fig. 2a). In this experiment, the stock solution was refilled after 5 days of experiment, and a possible slight difference in the composition of these two inlet solutions might have resulted in a correspondingly slight drop in outlet concentrations.

Overall, the cation release observed orthoclase stoichiometry in all experiments (Fig. 2b). Therefore, the few precipitates observed at the end of the MDA3 and MDA4 experiments (see below and Fig.S5) did not significantly affect the Al concentration measured in the fluid.

From the average concentrations measured at steady-state, orthoclase dissolution rates were calculated for each experiment (Eq. 1). These rates represent the average of the rates calculated from Si and K concentrations (Table 4), and range from 0.9 to 1.3 × 10^{-7} mol.m^{-2}.s^{-1}. Measurement reproducibility was therefore very good, given the uncertainties (~ 1- 2 × 10^{-8} mol.m^{-2}.s^{-1}).

Table 4. Orthoclase dissolution rates at 180 °C and pH 2 measured from MDA3, MDA4, MDA5, MDA6 and MDA7 experiments at far from equilibrium conditions (ΔG_r < -110 kJ.mol^{-1}).

	ΔGr (kJ.mol^{-1})	[Al] (mol.L^{-1})	r (10^{-7} mol.m^{-2}.s^{-1})
MDA3	-114	9.20E-06	1.2 ± 0.1
MDA4	-110	1.10E-05	1.2 ± 0.1
MDA5	-118	7.90E-06	1.3 ± 0.2
MDA6	-126	4.95E-06	0.9 ± 0.1
MDA8	-126	5.98E-06	1.1 ± 0.1

The average Al concentration and the Gibbs free energy of the reaction, two parameters known to impact the dissolution rate, are listed.

3.2 Experiments conducted on fresh powders under conditions of supersaturation with respect to secondary phases (experiments MPA)

3.2.1 Results of MPA-pH>2 experiments

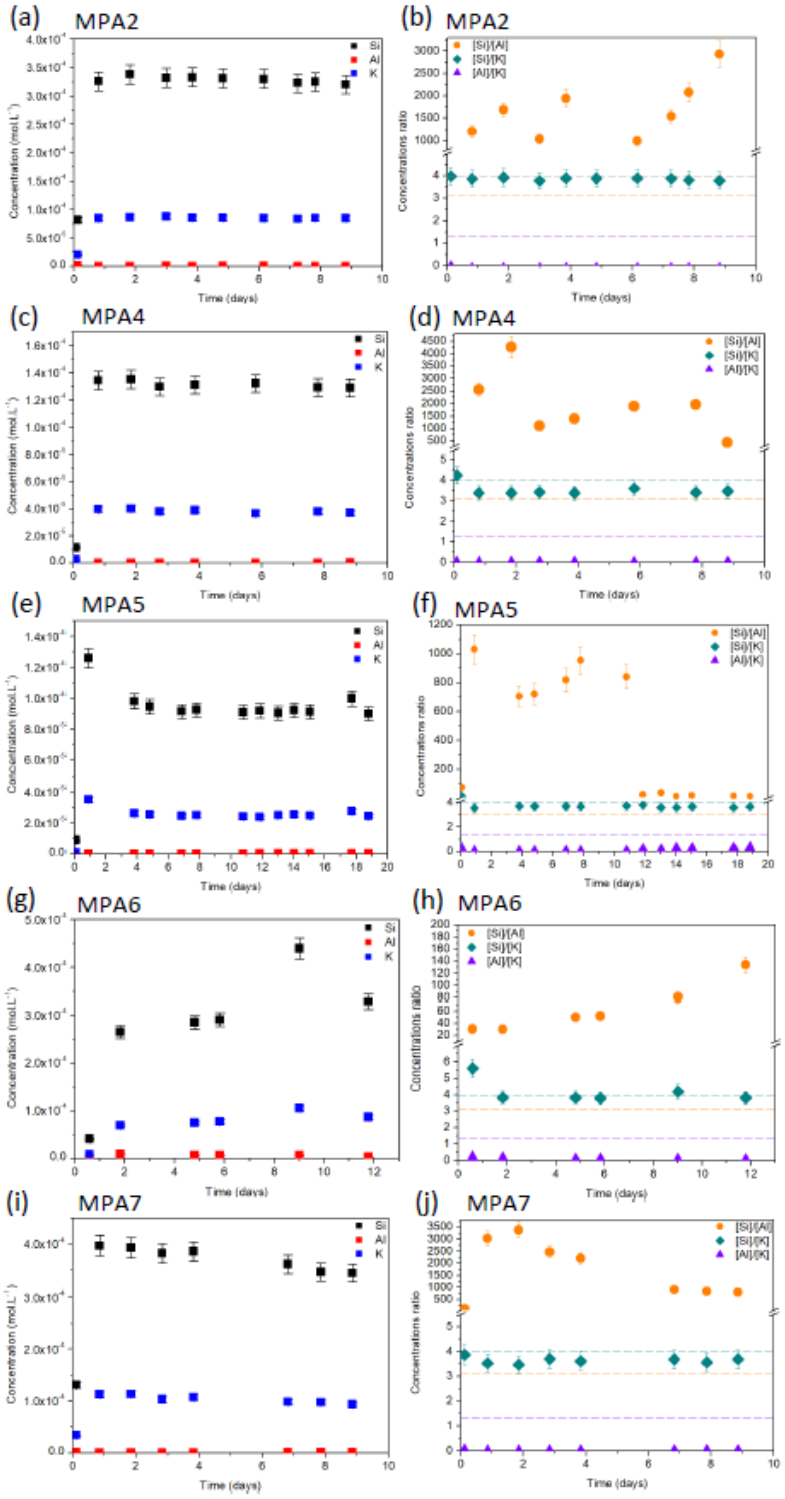

Fig. 3. Time-resolved fluid analyses of MPA-pH>2 experiments. (a, c, e, g, i) Time-resolved concentrations of released elements (outlet concentration subtracted from inlet concentration) and (b, d, f, h, j) ratios of these concentrations. The dashed lines represent the theoretical values of these ratios for stoichiometric dissolution.

The MPA-pH>2 experiments were carried out at pH > 2 and under conditions supersaturated with respect to Al-bearing phases. The [Si]/[Al] and [Al]/[K] ratios reveal a lack of Al in solution, resulting from the precipitation of Al-rich secondary phases.

The same treatment as presented in the previous section was carried out for experiments MPA2, MPA4, MPA5, MPA6 and MPA7. All these experiments were conducted at pH > 2, with the aim of forming a coating of secondary phases covering the orthoclase grains.

Figure 3 shows the differences between the measured outlet and inlet cation concentrations, which makes it possible to discuss the stoichiometry of the dissolution reaction (Fig. 3b). Aluminum depletion was observed in the fluid, as inferred from the [Si]/[Al] ratio, which is more than ten times higher than its theoretical value (3.1), while conversely, the [Al]/[K] ratio is very low (< 0.3) compared to its theoretical stoichiometric value (1.3). As the [Si]/[K] ratios are systematically close to their theoretical stoichiometric values (Fig. 3b), those results suggest that Al-rich secondary phases precipitated in these experiments, which was confirmed by the characterizations of the run products (see section *3.2.3*). The dissolution rates of orthoclase for these different experiments based on Si and K concentrations were calculated, and are listed in Table 5.

Table 5. Orthoclase dissolution rates at 180 °C and pH > 2 measured from experiments MPA2, MPA4, MPA5, MPA6 and MPA7 (MPA-pH>2).

	pH	ΔG_r (kJ.mol-1)	[Al] (mol.L-1)	r (10^{-7} mol.m^{-2}.s^{-1})
MPA2	3.1	-67	2.63E-07	0.39 ± 0.02
MPA4	4.3	-70	1.50E-07	0.16 ± 0.02
MPA5	4.7	-62	2.50E-06	0.11 ± 0.02
MPA6	3.8	-49	9.80E-06	0.27 ± 0.03
MPA7	3.0	-48	9.50E-07	0.47 ± 0.04

The pH, the Gibbs free energy of orthoclase dissolution (ΔG_r) and the average aluminum concentration are listed here. These parameters can influence the dissolution rate.

3.2.2 Results of MPA-pH2 experiments

Figure 4 shows the evolution of concentrations measured in experiments MPA1, MPA3, MPA8 and MPA9.

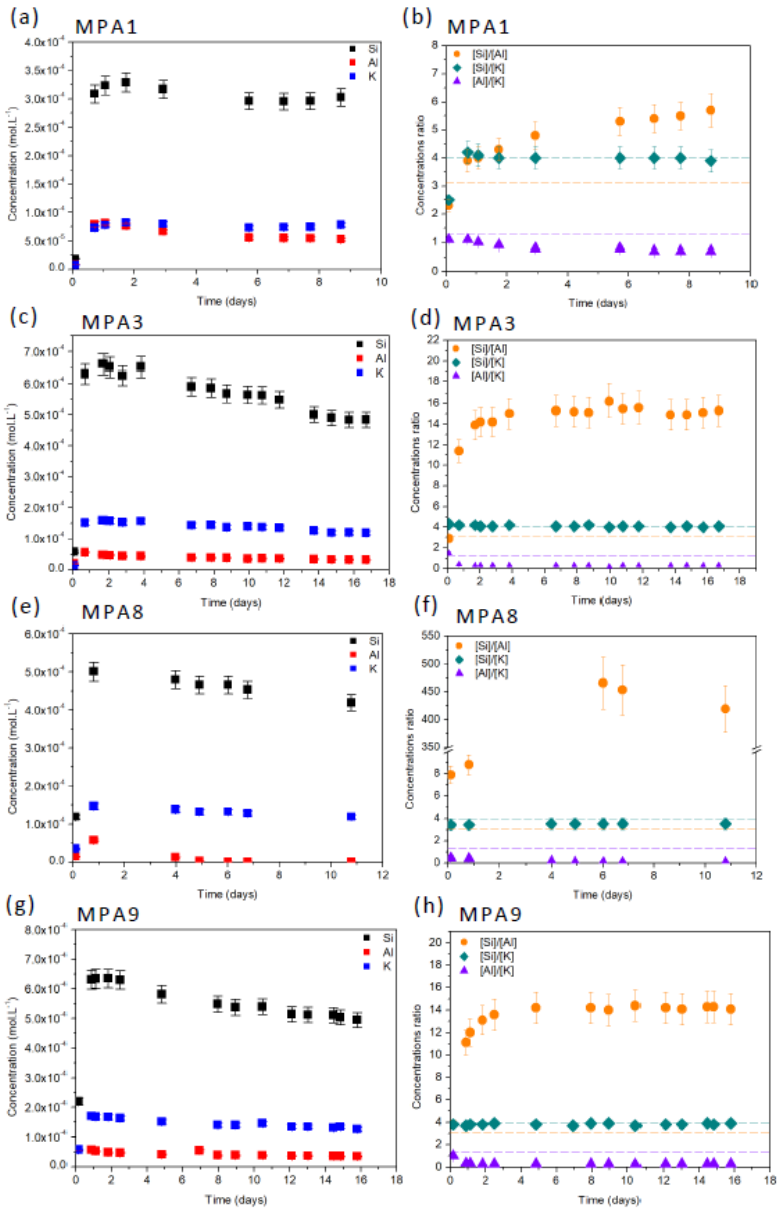

383

384 **Fig. 4. Time-resolved fluid analyses of MPA-pH2 experiments.** (a, c, e, g) Time-resolved concentrations of
385 released elements (outlet concentration subtracted from inlet concentration) and (b, d, f, h) ratios of these
386 concentrations. The dashed lines represent the theoretical values of the ratios calculated for stoichiometric
387 dissolution. The MPA-pH2 experiments were conducted at pH 2, under conditions supersaturated with respect to
388 Al-bearing phases. The [Si]/[Al] and [Al]/[K] ratios reveal a lack of Al in solution, resulting from boehmite
389 precipitation.

390

391 These experiments were carried out at pH = 2 using fresh powders, but under conditions
392 of supersaturation with respect to boehmite. The [Si]/[Al] and [Al]/[K] ratios indicate that the
393 solutions are depleted in Al, suggesting the precipitation of Al-rich secondary phases, which
394 was further confirmed by the characterizations of the run products (see section *3.2.3*). The

dissolution rates of orthoclase for these different experiments based on Si and K concentrations were calculated, and are listed in Table 6.

Table 6. Orthoclase dissolution rates at 180 °C and pH 2 measured from experiments MPA1, MPA3, MPA8 and MPA9 (MPA-pH2).

	ΔGr (kJ.mol^{-1})	[Al] (mol.L^{-1})	r (10^{-7} mol.m^{-2}.s^{-1})
MPA1	-72	6.42E-05	0.72 ± 0.03
MPA3	-66	3.40E-05	0.66 ± 0.07
MPA8	-64	3.50E-05	0.78 ± 0.07
MPA9	-63	4.14E-05	0.95 ± 0.07

The average Al concentration and the Gibbs free energy of the reaction, two parameters known to impact the dissolution rate, are listed.

3.2.3 Physicochemical properties of the coatings

3.2.3.1 Coating identification and structure

Figure 5 provides an overview of some orthoclase grains representative of the run products recovered at the end of the MPA experiments. It shows secondary precipitates partially (Fig. 5a-c) or totally (Fig. 5d) covering the surface of orthoclase grains.

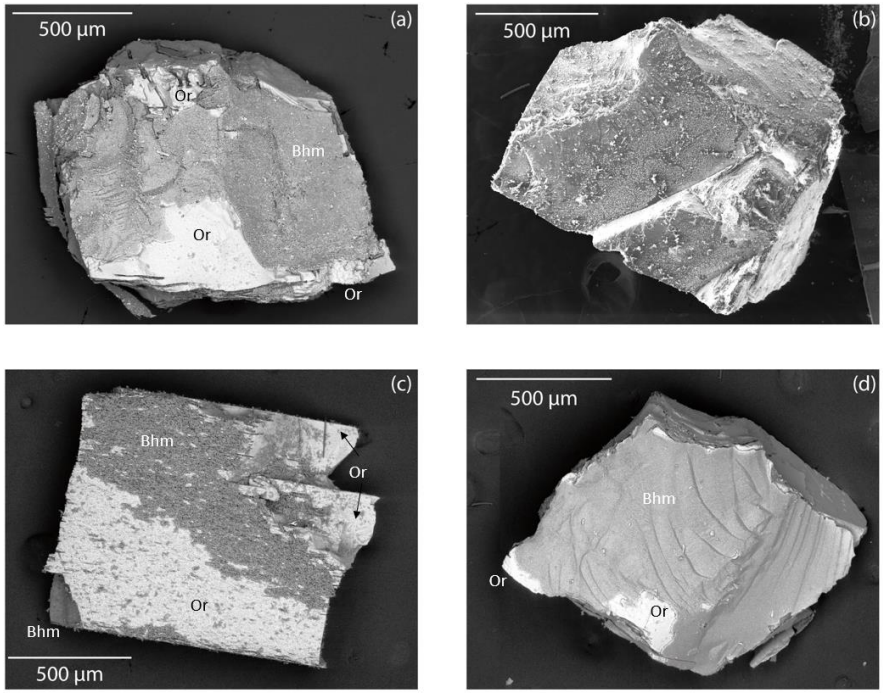

Fig. 5. Representative images of grains from experiments MPA-pH>2. The grains were collected from experiments (a) MPA2, (b) MPA4, (c) MPA5 and (d) MPA6. SEM images were taken either in SE (5b) or BSE (5a, c, d) mode. Orthoclase grains covered with secondary phase are visible. In the BSE images, the Al-rich phases appear darker than orthoclase.

XRD analyses of the powders from the MPA experiments showed that all secondary crystals consisted of boehmite (AlO(OH); see Fig. S6) whose chemical composition determined by EDXS is identical in all experiments, and whose shape and size was found to differ according to the chemical composition of the fluid (Fig. S7). This observation may be related to the saturation state of the fluid, which is known to control the respective rates of crystal nucleation and growth. If the fluid is only slightly supersaturated, the nucleation rate is low and the crystal growth process prevails. On the other hand, when the fluid is highly supersaturated, the nucleation process dominates at the expense of the growth process (see Daval et al., 2009b). In this case, numerous small crystals are observed. Moreover, the growth rates of the different faces of a crystal change as a function of the fluid saturation state, pH or composition (e.g., Dhanaraj et al., 2010; Godinho and Stack, 2015; Vital et al., 2020), possibly contributing to the diversity of crystal morphology revealed experimentally.

3.2.3.2 Grain surface coverage and coating thickness

Table 7. Main physical characterizations of boehmite coatings formed on orthoclase powders from MPA experiments (i.e., proportion of the powder surface covered with coatings and thickness of the coatings).

Experiment	Duration (days)	pH	Coverage (%)	Thickness (μm)
MPA1	9	2.1	20 ± 5	2.8 ± 0.1
MPA2	9	3.1	30 ± 5	2.2 ± 0.1
MPA3	17	2.1	22 ± 5	5.2 ± 0.1
MPA4	9	4.3	1.4 ± 0.5	0.8 ± 0.1
MPA5	19	4.7	11 ± 3	2.6 ± 0.1
MPA6	12	3.8	98 ± 2	1.2 ± 0.1
MPA7	9	3.0	55 ± 5	1.3 ± 0.1
MPA8	11	2.1	58 ± 5	3.9 ± 0.1
MPA9	16	2.1	7 ± 3	4.9 ± 0.1

The proportion of orthoclase powders covered by boehmite crystals as well as the thickness of the coatings are listed in Table 7. A strong correlation between reaction time and coating thickness was observed: for experiments carried out at pH 2, a linear relationship can be noticed between coating thickness and reaction time (Fig. S8). In addition, the lower the pH, the thicker the coatings. This later observation is consistent with the fact that the

dissolution rate of K-feldspar decreases when pH increases in the acidic pH range (Palandri and Kharaka, 2004), resulting in a larger release of Al for lower pHs.

Of note, some secondary coatings have proved brittle and do not stick firmly to the surface of orthoclase grains. Figure S9 shows that coatings sometimes partially detached from the surface of orthoclase grains. This was observed in particular in the MPA1, MPA3 and MPA9 experiments carried out at pH 2. As a result, the extent of coverage may be underestimated for these experiments. Of note, the powders recovered at the highest temperature (i.e. 95 °C, see section 2.2), with the exception of experiment MPA9, are those with the highest proportion of coatings. This might indicate that recovering powders at room temperature (the temperature at which boehmite is the most soluble) would partially damage the coatings. Finally, no clear correlation between the proportion of coverage and reaction time could be evidenced, a result which may be related to the brittleness and delamination of certain coatings.

3.2.3.3 Coating porosity

Porosity was measured on coatings from experiments MPA3 (conducted at pH 2), corresponding to the thickest coating, and MPA6 (conducted at pH 3.8), which exhibited almost 100% coverage.

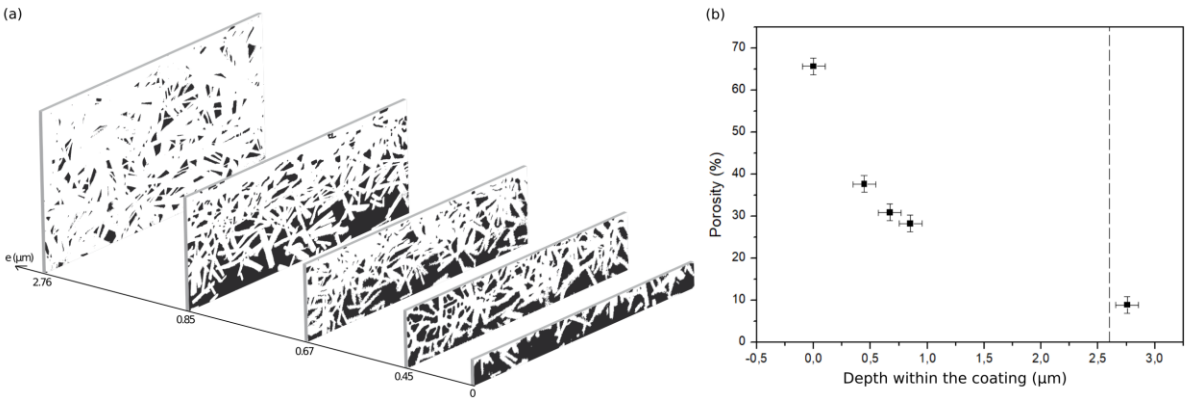

Fig. 6. An example of characterization of the porosity of boehmite coatings precipitated on orthoclase grains from MPA3 experiment. (a) Images of successive FIB cuts made in the secondary phase coating present on orthoclase grains. The *e* axis represents the coating thickness at which the cuts were made. The images were processed (grayscale thresholding) using ImageJ software to determine the porosity of the coating.

In the images, secondary phases appear in white and pores in black. (b) Porosity evolution within the boehmite coating formed on the grains in the MPA3 experiment. The coating has a total thickness of 5.2 µm. The dotted line represents the center of the coating. The point at x = 0 µm is at located at the contact with the solution.

Measurements were taken as a function of coating thickness on the grains from experiment MPA3, but only on the first half of the coating depth (Fig. 6a). The closer to the center of the coating, the lower the porosity (Fig. 6b). In contrast, the thickness of the coating on the grains from the MPA6 experiment is too thin for depth-dependent measurements. As a consequence, for this experiment, an average porosity was measured from the various cross-sections made within the coatings, and estimated at 22 ± 5% on average.

In the next section, the results of dissolution experiments carried out at pH 2 on powders initially coated with boehmite (experiment MDAc) are described. These powders were recovered from experiments MPA2, MPA4, MPA5, MPA6 and MPA7 (MPA-pH>2).

3.3 Experiments conducted at pH 2 on boehmite-coated powders in solutions supersaturated with respect to secondary phases (experiments MDAc).

3.3.1 Dissolution rates

Figure 7 shows the concentrations of elements released from orthoclase dissolution in the MDAc experiments. The Al concentration in experiments MDA7, MDA9 and MDA11 was found to be very low. The [Si]/[Al] and [Al]/[K] ratios do not correspond to the stoichiometric ratios of orthoclase (Fig. 7b), indicating the precipitation of Al-rich secondary phases. Conversely, the [Si]/[Al] and [Al]/[K] ratios of the MDA10 experiment are close to their theoretical stoichiometric ratios, indicating that no massive reprecipitation of secondary phases took place in this experiment. Finally, experiment MDA12 shows a drop in Al concentration after ~10 days, which may correspond to the onset of Al-bearing phase precipitation. From the measured Si and K concentrations, the dissolution rates of orthoclase dissolution were calculated for all experiments, and are listed in Table 8.

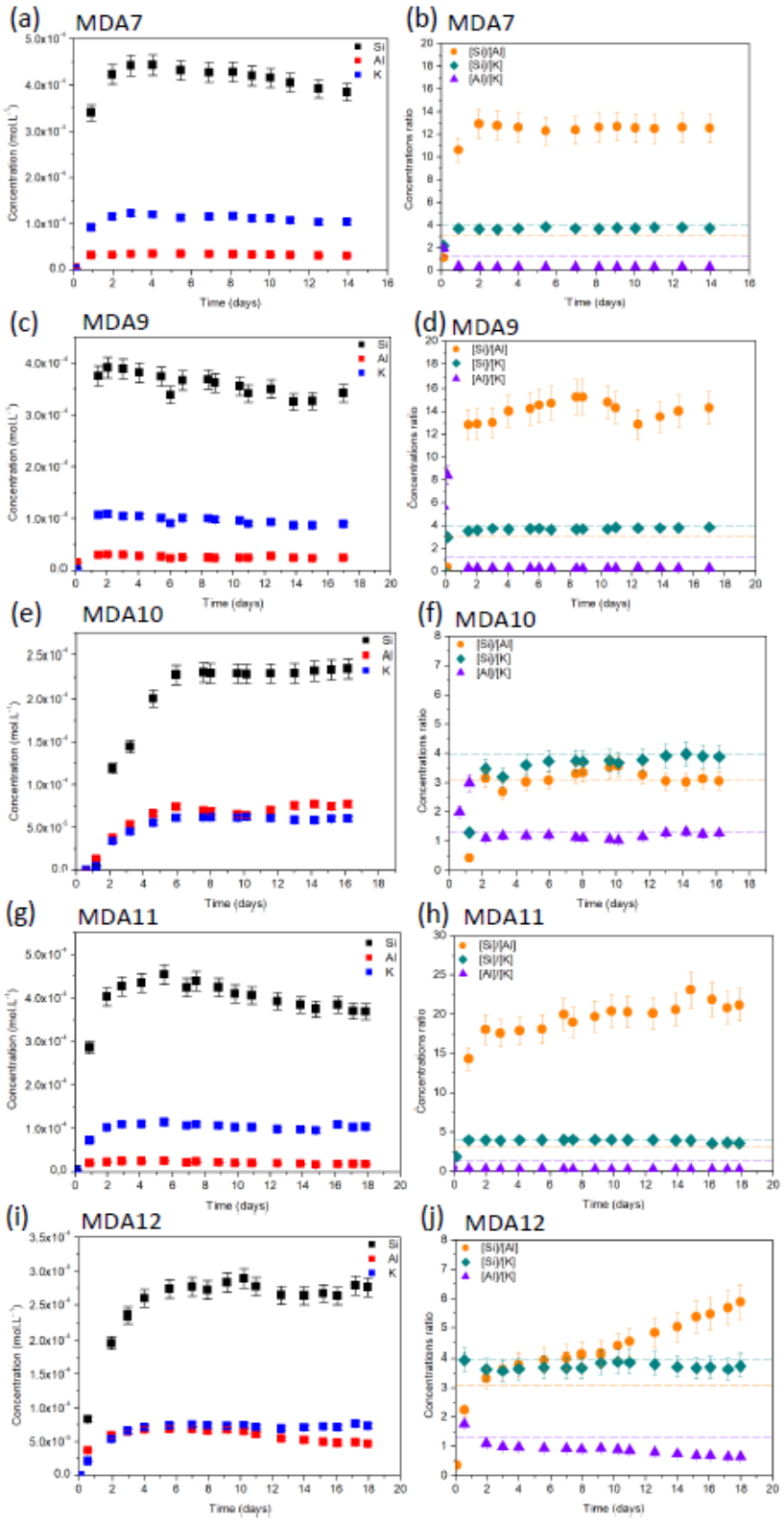

Fig. 7. Time-resolved fluid analyses of MDAc experiments. (a, c, e, g, i) Time-resolved concentrations of released elements (outlet concentration subtracted from inlet concentration) and (b, d, f, h, j) ratios of these concentrations. The dashed lines represent the theoretical values of the ratios calculated for stoichiometric dissolution. The MDAc experiments were carried out at pH 2 and under conditions supersaturated with respect to Al-bearing phases. The [Si]/[Al] and [Al]/[K] ratios reveal a lack of Al, resulting from boehmite precipitation.

Table 8. Measured dissolution rates for MDAc experiments conducted at pH 2, using powders covered with boehmite coatings resulting from MPA-pH>2 experiments.

Experiment	Starting materials	ΔGr (kJ.mol^{-1})	[Al] (mol.L^{-1})	r (10^{-7} mol.m^{-2}.s^{-1})
MDA7	MPA6	-69	5.92E-05	0.64 ± 0.05
MDA9	MPA5	-71	4.29E-05	0.60 ± 0.05
MDA10	MPA7	-74	7.52E-05	0.36 ± 0.02
MDA11	MPA4	-78	4.51E-05	0.70 ± 0.04
MDA12	MPA2	-72	6.80E-05	0.46 ± 0.02

The starting powders are indicated in the second column. In the last three columns, the Gibbs free energy of orthoclase dissolution, the Al concentration and the dissolution rates are listed.

3.3.2 Coating properties at the end of the experiments

At the end of the MDAc experiments, the powders were analyzed by SEM (Fig. S10). The extent of grain coverage after the MDAc experiments is below 10%, and virtually zero for some powders (e.g. Fig. S10a). The powders used for the MDAc experiments are those issued from the MPA-pH>2 experiments. It can be seen that the grains had a greater coverage before their re-dissolution at pH 2 (Table 7 and Figure 5). This would therefore indicate that part of the boehmite coating was lost either during the MDAc experiments or at the end of the experiments. However, both the aqueous elemental ratios and the thermodynamic calculations based on Al concentration (Fig. 7) indicate that Al-rich phases did indeed precipitate during the MDAc experiments. Two hypotheses can be offered to explain these observations:

(1) Secondary coatings came off before or during the MDAc experiments. New precipitates were formed in the autoclave, but not at the surface of orthoclase grains;

(2) The coatings came off at the end of the MDAc experiments, during recovery of the run products.

As a consequence, one has to keep in mind that the interpretations of these experiments will differ depending on the actual scenario that took place during the experiments. Indeed, it is possible that the dissolution rates measured during the MDAc experiments are relative to

boehmite-coated powders or not. The MPDA experiment was designed to circumvent these problems.

3.4 MPDA experiment

Figure 8a shows the concentrations of elements released during orthoclase dissolution, together with the ratios of these concentrations. Two stages (referred to as MPDAa and MPDAb) can be clearly distinguished during the experiment. The first one corresponds to the alteration of orthoclase at pH 4 in a solution highly supersaturated with respect to aluminum hydroxides. The second one, which began 11 days after the onset of the experiment, corresponds to the dissolution of the powder at pH 2. Concentrations were found to be higher in the MPDAb stage, as orthoclase dissolution rate is higher at pH 2 than at pH 4. However, while a steady-state can be observed during the MPDAa phase, sharp variations in concentrations were observed at the end of the experiment. These variations may be due to the precipitation/redissolution of other secondary phases containing Si and K, or to the possibility that the dissolution rate of orthoclase is not constant under these conditions.

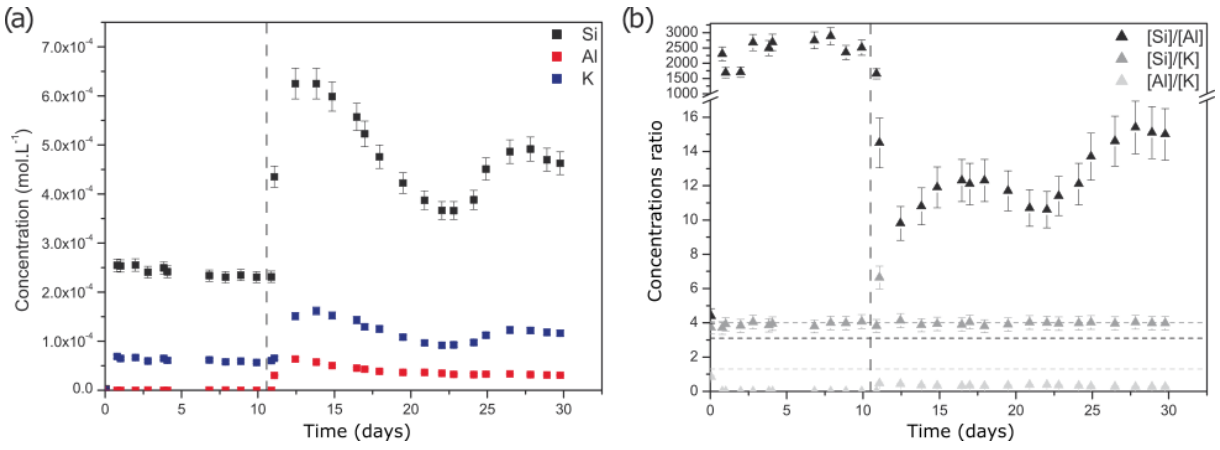

Fig. 8. Time-resolved fluid analyses of MPDA experiment. (a) Time-resolved concentrations of released elements (outlet concentration subtracted from inlet concentration) and (b) ratios of these concentrations. The dashed lines represent the theoretical values of the ratios calculated for stoichiometric dissolution.

Figure 8b shows that stoichiometry was respected for Si and K concentrations. On the other hand, Al was released incongruently, suggesting its precipitation in secondary phases

throughout the experiment. Typical orthoclase grains representative of the run products at the end of the MPDA experiment are shown in Fig. 9. The grains are almost totally covered with boehmite (90% surface coverage), suggesting that powder handling at the end of the experiment may not affect the extent of the grain coverage. Although these observations do not allow us to draw definitive conclusions with respect to the (at least partial) lack of coatings in the MDAc experiments, it thus seems impossible to rule out the possibility that the coatings were damaged during the MDAc experiments, and more particularly when they were introduced into the reactor at the start of the experiment (hypothesis 1, section *3.3.2*). The presence of the coatings during the MDAc experiments therefore remains uncertain.

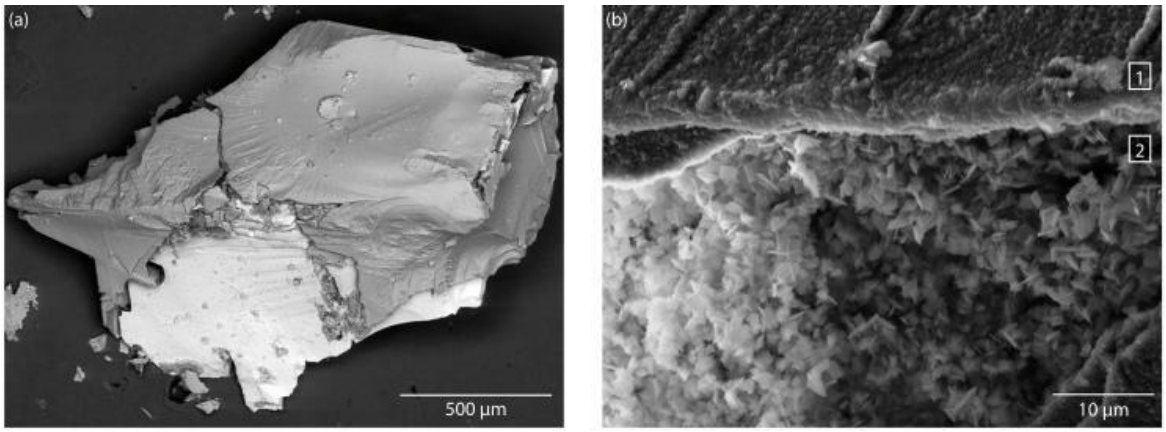

Fig. 9. SEM images of grains from the MPDA experiment. (a) BSE image of orthose grains are heavily coated with secondary phases. (b) SE image at higher magnification of secondary coatings. Two different textures (marked 1 and 2), already observed in the MPA experiments (Fig. S7), can be evidenced.

Referring back to the MPDA experiment, the crystals that make up the coatings were observed to have two different sizes and morphologies (Fig. 9b), which were already observed in the MPA experiments (Fig. S7). These differences may be ascribed to the precipitation of two successive generations of boehmite coatings formed at pH 4 and pH 2, respectively. Their thickness was measured to be 2.0 ± 0.2 µm on average. No secondary phases other than boehmite was detected in the run products. This observation implies that the variations in concentration observed during the MPDAb step can only be linked to a variation

552 in the rate of orthoclase dissolution. This variation may be due to the successive
553 precipitation/dissolution of boehmite during the experiment.

554 Based on the measured concentrations, the average dissolution rate of orthoclase during
555 the first stage of the experiment (performed at pH 4) is estimated at $(0.27 \pm 0.01) \times 10^{-7}$
556 $mol.m^{-2}.s^{-1}$. Despite the variations in concentration observed during the second step performed
557 at pH 2, the dissolution rate of orthoclase under these conditions can be estimated to range
558 between 0.42×10^{-7} and 0.68×10^{-7} $mol.m^{-2}.s^{-1}$, with a mean value of $(0.54 \pm 0.09) \times 10^{-7}$
559 $mol.m^{-2}.s^{-1}$ (the error corresponds to the standard deviation of the measurements made).

560 **3.5 Brief summary of the results**

561 In the MPA experiments, boehmite coatings formed on the surface of orthoclase grains.
562 By varying pH and/or reaction time, coatings of different texture, thickness and surface
563 coverage were formed. A comparison of dissolution rates measured at pH 2 on coated
564 powders (experiments MPA-pH2, MDAc and MPDA) and powders not coated with
565 secondary phases (experiments MDAf) provides information on the effect of coatings on
566 orthoclase dissolution kinetics.

567 When the powders were recovered at the end of the MDAc experiments, most of the
568 grains were no longer coated with secondary phases. The coatings may have dissolved or
569 detached from the grains during the dissolution experiments or when the powders were
570 collected at the end of the experiments. Uncertainty therefore remains as to the presence of
571 coatings during these experiments. On the other hand, boehmite coatings were found at the
572 end of the MPA-pH2 and MPDA experiments.

573 The dissolution rates measured for each series of experiments are listed in Table 9. It can
574 be seen that dissolution rates measured on fresh powder in the absence of secondary coatings
575 (experiments MDAf) are higher than those measured on boehmite-coated powders. The
576 coating of secondary phases could therefore be responsible for a drop in the dissolution rate of

orthoclase. However, other factors, such as the chemical affinity of the reaction and the aluminum concentration in the reactor, can also result in a drop in reactivity. The influence of each of these parameters is discussed below.

Table 9. A summary of orthoclase dissolution rates measured during the different series of experiments carried out at 180 °C and pH 2. The

Experiment	r (10^{-7} mol.m^{-2}.s^{-1})
MDAf	0.90 – 1.30
MPA-pH2	0.66 – 0.95
MDAc	0.36 – 0.70
MPDAb	0.42 – 0.68

MDAf experiments were conducted using fresh powders, in the absence of secondary phases. In the MPA-pH2 experiments, boehmite precipitated on the surface of orthoclase grains. The MDAc experiments were carried out on powders coated beforehand with boehmite. The MPDAb experiment corresponds to the alteration of boehmite-coated powder in which the grains were not dried or manipulated between the coating formation stage and the dissolution stage at pH 2.

4. Discussion

In this study, variations in the dissolution rate of orthoclase may be due to the presence of secondary phases, which could mask part of the reactive surface of the grains and/or favor the development of microenvironments with fluid composition deviating from that of the bulk fluid. However, two other parameters, i.e., the Gibbs free energy (ΔG_r) of the reaction (Burch et al., 1993; Gautier et al., 1994; Hellmann and Tisserand, 2006; Hellmann et al., 2010; Pollet-Villard et al., 2016b) and the Al concentration in the bulk fluid (Gautier et al., 1994; Oelkers et al., 1994) may have also contributed to the rate decrease. These hypotheses are discussed below.

4.1 Influence of the Gibbs free energy of reaction on orthoclase dissolution rate

For over 30 years, several studies have demonstrated that mineral dissolution rates do not simply follow rate laws derived from the transition state theory (TST). Whereas TST-based

rate laws predict that the dissolution rate of a given chemical process is virtually unaffected by the distance to equilibrium as long as ΔG_r < ~ -20 kJ/mol, a dramatic drop in the dissolution rate was actually observed experimentally for various minerals at much lower values (Daval et al., 2010; Taylor et al., 2000; Burch et al., 1993; Hellmann and Tisserand, 2006; Hellmann et al., 2010). Regarding orthoclase, Pollet-Villard et al., 2016a suggested that a drop in orthoclase dissolution rate could be observed for values as low as ~ -68 kJ.mol^{-1}.

In the MDAf experiments, the Gibbs free energy of orthoclase dissolution is consistently below -110 kJ.mol^{-1}. There is therefore no influence of ΔG_r on the dissolution rates calculated in these experiments. Regarding MPA-pH2 experiments, ΔG_r varies from -72 to -63 kJ.mol^{-1}. Accordingly, this variation can only result in a very modest decrease in reactivity, on the order of 1% at most, based on the empirical relations proposed in Pollet-Villard et al., 2016a. Such an impact remains much lower than the uncertainties on measured concentrations (5-10%). Finally, all MDAc experiments and the MPDA experiment (second step) were carried out at $\Delta G_r \leq$ -67 kJ.mol^{-1}, such that the fluid saturation state should have not influenced orthoclase dissolution rate.

Overall, it can therefore be concluded that any difference in terms of orthoclase reactivity between the various experiments could not be ascribed to the Gibbs free energy of orthoclase dissolution.

4.2 Influence of aqueous Al concentration on orthoclase dissolution rates

According to several studies, aqueous Al may inhibit the dissolution rate of feldspars (e.g., Gautier et al., 1994; Oelkers et al., 1994; Oelkers, 2001). At far from equilibrium conditions and in the acidic pH domain, the dependence of feldspar dissolution rate on the activity of Al^{3+} has been suggested to observe:

$$r = k_d . \left(\frac{a_{H+}}{a_{Al3+}} \right)^q \quad (5)$$

where a_i represents the activity of species i and k_d a dissolution constant. The value of q was proposed to depend on the stoichiometry of a so-called 'activated complex' or 'surface precursor', with a value equal to -1/3 for K-feldspar (Gautier et al., 1994). To test the possible impact of Al in our experiments, the logarithm of the dissolution rate was plotted as a function of the logarithm of Al concentration measured in the solution (Fig. 10). The rate data observe a negative correlation with Al concentration. Despite a rather low correlation coefficient (R^2 = 0.65), the slope of the linear regression (-0.31) is in very good agreement with the value of -1/3 predicted by Eq. (5).

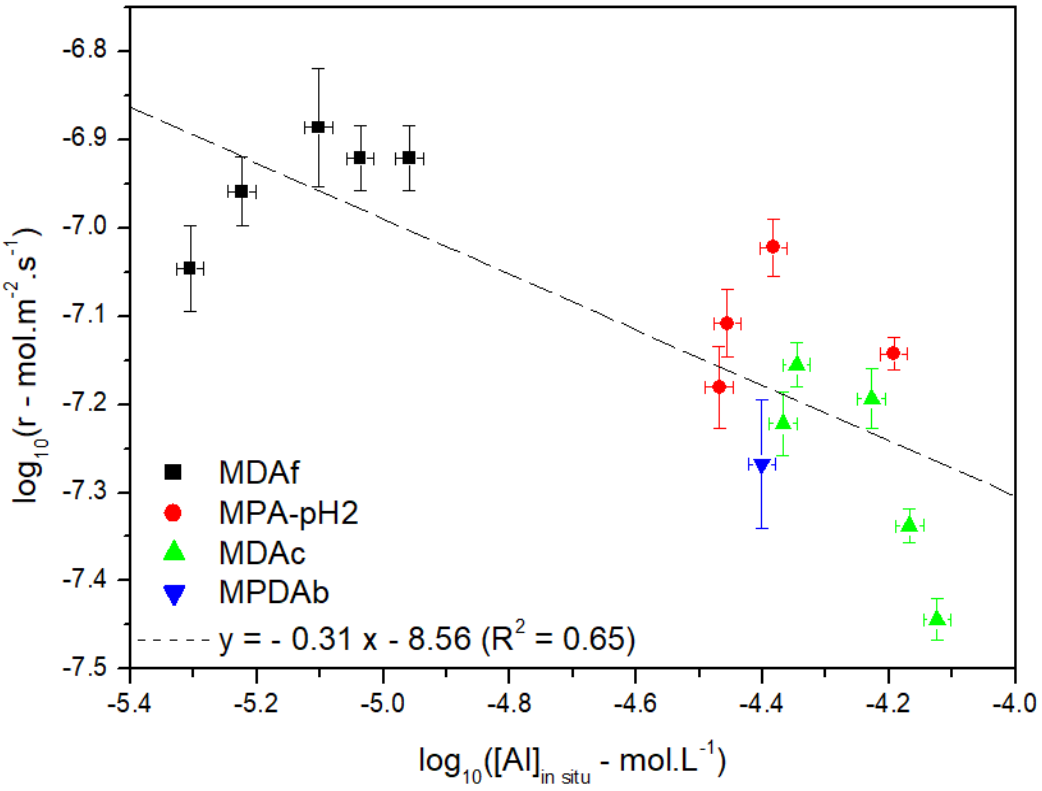

Fig. 10. Logarithm of orthoclase dissolution rates measured at pH 2 as a function of the logarithm of Al concentration in solution. The dashed line corresponds to a linear regression of the data. The slope of the line is equal to -0.31. According to Gautier et al., 1994, the theoretical value of the slope is equal to -1/3. See text for details.

To better appreciate the contribution of Al aqueous concentration on orthoclase reactivity, dissolution rates were recalculated using Eq. (5) and an arbitrary Al concentration equal to 10^{-5} mol.L^{-1} (Table 10). As can be seen, whereas the recalculated dissolution rate of

fresh orthoclase powders (i.e., not covered with secondary coatings) range from 0.9 to 1.2 × 10^{-7} mol.m^{-2}.s^{-1}, the recalculated dissolution rates of coated orthoclase powders range from 0.7 to 1.5 × 10^{-7} mol.m^{-2}.s^{-1}. With the possible exception of experiment MDA10, if aqueous Al does contribute to the decline in orthoclase reactivity, then the dissolution rate of fresh and coated powders overlap. Therefore, and although it should be reminded that the theoretical and experimental validity of Eq. (5) has been extensively questioned in the literature (e.g., Luttge, 2006), it follows from such calculations that the effect of secondary coatings could be considered negligible. In the next section we test whether the slight difference in reactivity between coated and uncoated orthoclase powders could alternatively be explained by some physical characteristics of the secondary coatings.

Table 10. Orthoclase dissolution rates at 180°C and pH 2 measured from MDAf, MPA-pH2, MDAc and MPDA experiments and recalculated for an Al concentration of 10^{-5} mol.L^{-1} using Eq. (5).

Experiment		r_{corr} (10^{-7} mol.m^{-2}.s^{-1})
MDAf	MDA3	1.2 ± 0.1
	MDA4	1.2 ± 0.1
	MDA5	1.2 ± 0.2
	MDA6	0.7 ± 0.1
	MDA8	0.9 ± 0.1
MPA-pH2	MPA1	1.30 ± 0.03
	MPA3	1.00 ± 0.07
	MPA8	1.20 ± 0.07
	MPA9	1.50 ± 0.07
MDAc	MDA7	1.16 ± 0.05
	MDA9	0.97 ± 0.05
	MDA10	0.71 ± 0.02
	MDA11	1.16 ± 0.04
	MDA12	0.87 ± 0.02
MPDA	MPDAb	0.86 ± 0.09

4.3 Influence of coatings on orthoclase dissolution rates

To highlight a possible relation between orthoclase reactivity and the presence of secondary coatings, graphs representing the rates of orthoclase dissolution, using rates either

uncorrected for the impact of Al (r) or taking into account a possible impact of Al (r_{corr}), were plotted as a function of the proportion of surface covered and the thickness e of the coatings respectively, both measured at the end of the experiments (Fig. 11). Note that the MDAf experiments (black squares in Fig. 11) were carried out in the absence of secondary phases throughout the experiments while conversely, the MPA-pH2 experiments (red circles) were free of coatings only at the beginning of the experiments. In contrast, the MDAc experiments (green triangles) were carried out on powders initially covered with secondary phases (starting powders coming from the MPA-pH>2 experiments).

Overall, the dissolution rate of coated powders is generally lower than the dissolution rates measured in the absence of a secondary phases, with an apparent decrease in reactivity of around 44% (Figs. 11a and b). Conversely, and as suggested in the previous section, accounting for a possible impact of Al on orthoclase reactivity results in dissolution rates that no longer depend on the properties of the orthoclase powders (coated with secondary coatings or not). No clear trend that would relate the dissolution rates to the proportion of surface covered and/or the thickness e of the coatings can be evidenced.

Overall, the results suggest that secondary phases formed on orthoclase grains have no major influence on dissolution rates. A modest decrease in reactivity of the order of 40% is observed when the grains are covered with boehmite, which could also be attributed to the inhibiting effect of aluminum in solution. Interestingly, the present study confirms the results reported in several previous experimental efforts focused on coupled dissolution-precipitation reactions. For instance, Hellmann et al., 1989 observed that the formation of 100s µm-thick boehmite coatings on albite crystals altered at pH 2.4 and 300 °C had a negligible impact on albite dissolution rates. Studies aimed at unravelling the impact of carbonate formation throughout water-silicate-CO_2 interactions on the rate and yield of silicate carbonation have also reported only a modest decrease in silicate reactivity (e.g., Stockmann et al., 2008; Daval

et al., 2009a; Stockmann et al., 2011; Saldi et al., 2013; Stockmann et al., 2013). For all those studies, including the present one, a striking common feature is the lack of crystallographic relationship between the parent phase and the secondary phases, whereas Cubillas et al., 2005 proposed that a crystallographic template adapted for epitaxial growth could be a prerequisite to efficiently decreasing primary mineral dissolution rates. Contrasting with this suggestion, the reactive-transport simulations conducted by Emmanuel, 2022 showed that some properties of the coatings that are not related to the crystalline structure of the parent phase and/or the secondary coatings are critical in controlling the reactivity of the parent phase and in particular, (i) the thickness and (ii) the porosity/tortuosity ratio inside the coatings. Following a similar approach, we explore numerically in the next section whether the specific physical properties of the boehmite coatings reported above were likely to act as a barrier to ion diffusion from mineral to solution (and vice versa), and thus assess independently the impact of these coatings on orthoclase dissolution rates.

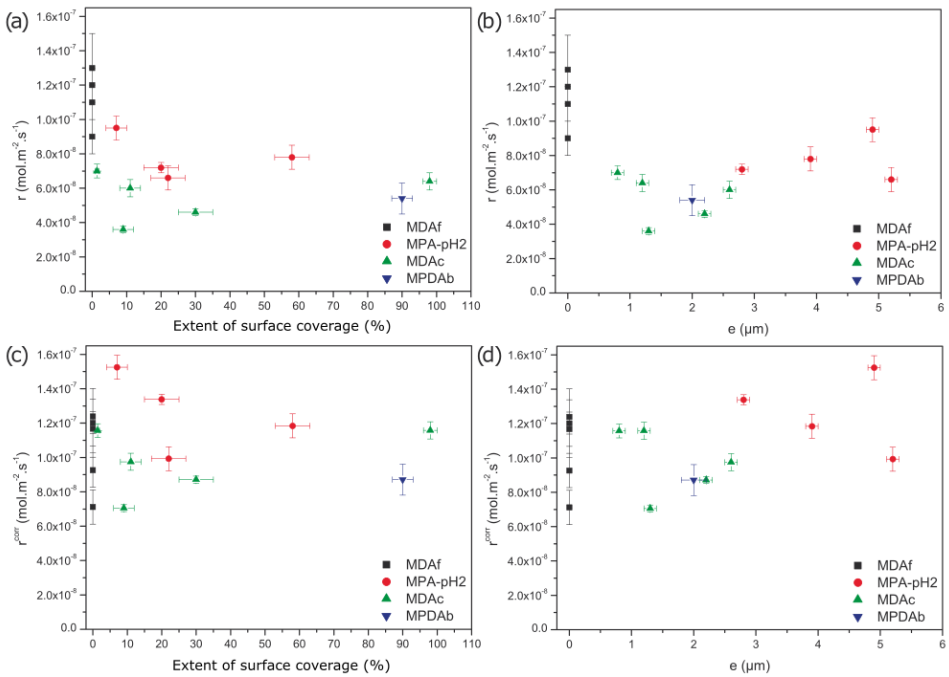

Fig. 11. Relation between dissolution rates *r* measured at pH 2 and (a) the extent of surface coverage and (b) coating thickness *e* (µm). The same graphs ((c) and (d)) were plotted considering r_{corr} instead of *r*, which have been recalculated at an Al concentration arbitrarily set at a value of 10^{-5} mol.L^{-1}.

4.4 Contribution of reactive transport modeling

As mentioned above, the secondary coatings formed on the surface of orthoclase do not seem to act as a diffusion barrier, nor isolate the orthoclase surface from the bulk fluid, as suggested by the modest decrease in K-feldspar reactivity measured experimentally (see Sections 4.1-4.3). The question arises as to whether such results are compatible with and/or could have been predicted based on the physical properties of the coatings. The 1D reactive transport model described in Section 2.4 and parameterized following the physical characterizations described above was used address this question. The simulations were used to calculate the flux of H^+ ions through the coatings and estimate the characteristic time required for H^+ ions to pass through the coatings, as well as the pH at the boundary between the primary mineral and the coating. An estimate of the apparent dissolution rate of the mineral could then be calculated as a function of the coatings' characteristics of experiments MPA6 and MPA3, for which the characterization of the coatings was the most extensive. Finally, the model was also used to explain why coatings may significantly affect very reactive phases such as calcite, while their effect on orthoclase alteration is negligible.

4.4.1 Model outputs for experiment MPA6

Regarding experiment MPA6, both the porosity φ and the effective diffusion coefficient D were assumed to be constant within the coating. With a porosity of 22%, the effective coefficients $D_{m=2.0}$ and $D_{m=1.5}$ are equal to 1.6×10^{-9} and 3.4 × 10-9 $m^2.s^{-1}$, respectively (Eq. 3). Figure 12 shows the H^+ concentration profiles ($C(x)$) within the coating for different times t, both for m = 1.5 and m = 2. In addition, the evolution of H^+ concentration as a function of time in the C_N cell, which is in contact with orthoclase, is depicted in Figure 13. It can be seen that the proton concentration in the coating quickly reaches a steady state (for t < 1 ms). The concentration in the cell in contact with orthoclase (C_N) then reaches a steady-state value corresponding to $0.98C_0$, i.e., pH = 2.01 (using pH_0 = 2.00). Assuming that the dissolution

rate of orthoclase at pH 2.00 is r_0 = 1.00 × 10^{-7} mol.m^{-2}.s^{-1}, the dissolution rate of orthoclase coated with secondary phases would be 0.99 × 10^{-7} mol.m^{-2}.s^{-1}, considering a reaction order of n = 0.5 with respect to a_{H+}. Under these conditions, the decrease in reactivity would be too weak to be detected. Therefore, the model constrained with the physical properties of the secondary coatings independently confirms the conclusions reached in the previous sections: the impact of secondary coatings was negligible throughout the experiment.

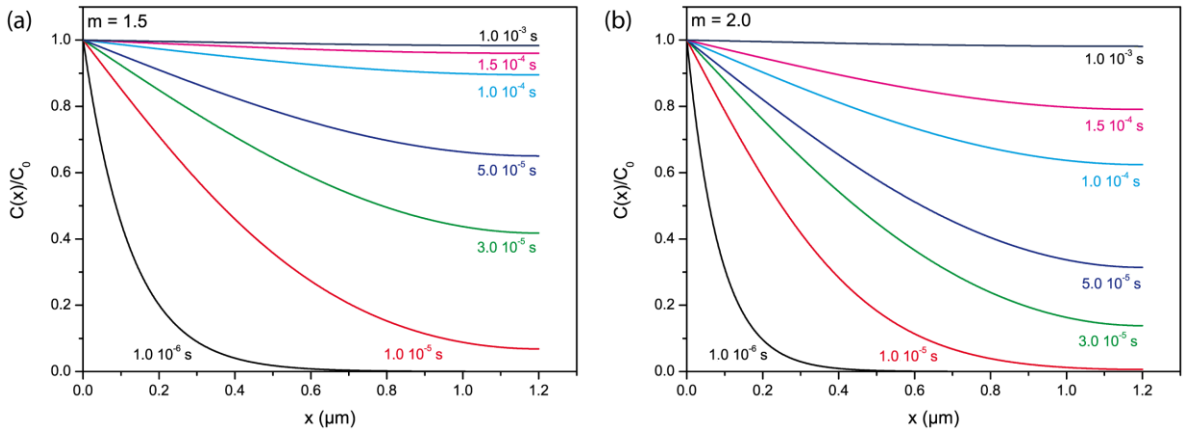

Fig. 12. Evolution of the $C(x)/C_0$ ratio in the coating of experiment MPA6 at different times t (s), for simulations performed with (a) m = 1.5 and (b) m = 2.0, respectively.

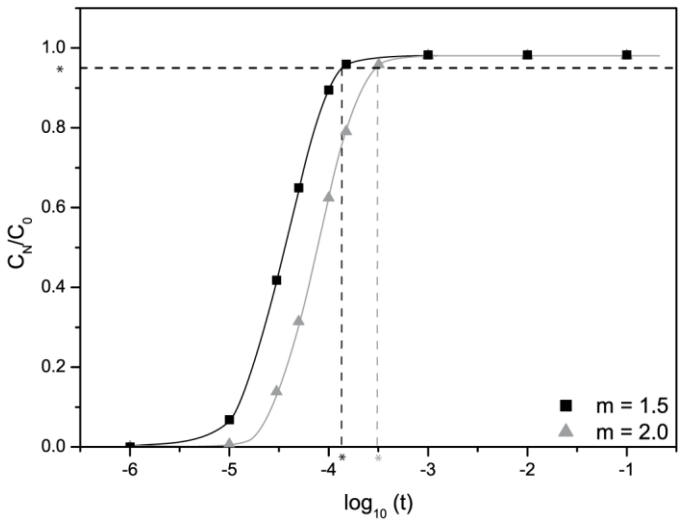

Fig. 13. Evolution of the C_N / C_0 ratio as a function of log(t) for m = 1.5 (black curve) and m = 2.0 (gray curve). C_N represents the H^+ concentration in the last N cell of the coating, t (s) is the diffusion time within the coating. The star (∗) marks the time after which C = 0.95C_0.

740 In addition, because the choice of m has little influence on the results, we have chosen to run
741 the subsequent simulations with m = 2.0. This corresponds to the case where D is the lowest,
742 and therefore, the condition under which the buildup of a diffusion boundary layer within the
743 coating is the most likely.

744 *4.4.2 Model outputs for experiment MPA3*

745 In the MPA3 experiment, porosity decreases from the coating/fluid interface inwards
746 (Fig. 6b). Note that the porosity of the coating at a depth exceeding 2.6 µm could not be
747 measured. For the numerical simulations, it was assumed that for x > 2.6 µm, the porosity
748 remained equal and constant to that measured at x = 2.6 µm. The profile of the effective
749 diffusion coefficient $D(x)$ within the coating (Fig. 14a) was then calculated from Archie's law
750 (Eq. 3). Under such conditions, when the H^+ concentration profile reaches steady-state
751 conditions, the H^+ concentration in the cell contacting the orthoclase surface corresponds to
752 $C_N = 0.89C_0$ (Fig. 14b). The apparent dissolution rate of orthoclase in this case is 0.94×10^{-7}
753 $mol.m^{-2}.s^{-1}$, which is impossible to distinguish experimentally from the expected rate at pH =
754 2. In addition, the duration required to reach a steady-state H+ profile within the coating is
755 negligible compared to the duration of the experiment ($t^* = 1.7 \times 10^{-2}$ s), so that the impact of
756 the coating on the orthoclase dissolution rate was not significant for experiment MPA3.
757 Consequently, the slight loss of reactivity reported previously might be better explained by
758 the Al inhibition previously suggested in the literature for feldspars (Gautier et al., 1994;
759 Oelkers et al., 1994) rather than by ion diffusion limitation in the coating.

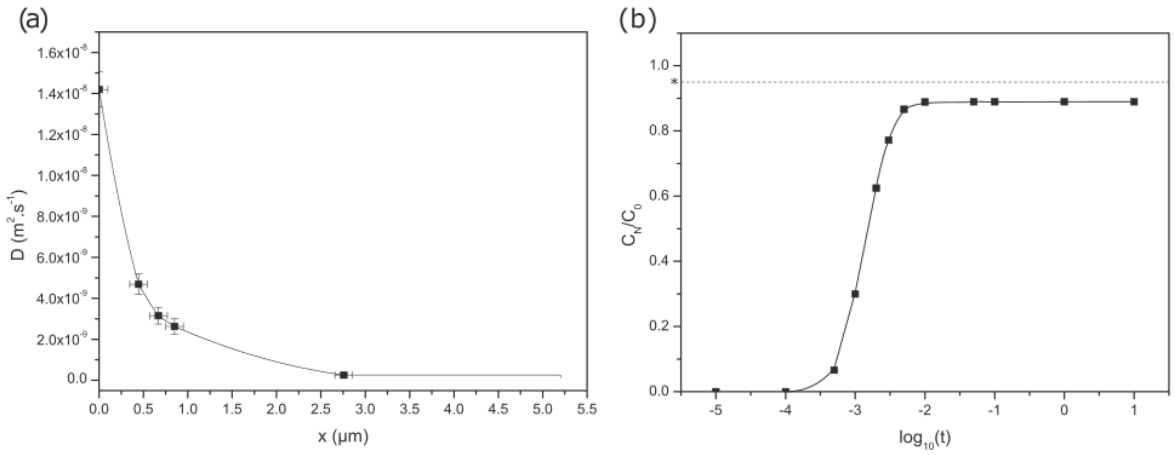

Fig. 14. Main results for the reactive transport modeling of experiment MPA3. (a) Diffusion coefficient across the coating thickness estimated following Archie's law. (b) Evolution of the C_N / C_0 ratio as a function of log(t) for m = 2.0. C_N represents the H^+ concentration in the last N cell of the coating, t (s) is the diffusion time within the coating.

4.4.3 Sensitivity tests

In order to determine the conditions under which coatings could affect the dissolution rate to a greater extent, additional simulations were carried out. Two parameters were considered in particular, i.e., the thickness of the secondary coatings and the pH of the bulk fluid. For geothermal systems, such parameters are particularly relevant to estimate the impact of the coatings on the longer term: on the one hand, the pH of circulating waters will gradually return to its value before the acid stimulation, while on the other hand, it can also be expected that the thickness of the coatings will gradually increase with time. Finally, the impact of the intrinsic dissolution rate constant of the mineral considered will also be investigated, to shed light on the impact that secondary coatings may have on minerals more reactive than K-feldspars.

All simulations were carried out considering a homogenous coating (i.e., φ and D independent of x), using time and space increments of $\Delta t = 10^{-5}$ s and Δx = 1 nm, respectively. The characteristic time (t_{eq}) required to reach steady-state conditions (constant C_N concentration) was systematically lower than t_{max} = 10 s, and therefore negligible compared

781 with the duration actually simulated. As emphasized previously, the key parameter for
782 estimating the effect of coatings on the dissolution rate of orthoclase is the concentration of
783 H^+ ions in the last cell of the coating when the steady-state is reached.

784 *4.4.3.1 Influence of pH*

785 In order to simulate conditions closer to those of the Soultz-sous-Forêts reservoir at the
786 end of an acid stimulation, the model was run with a bulk fluid at pH = 5.3, corresponding to
787 that of the brine measured on-site (e.g., Sanjuan et al., 2010).

788 Considering the pH-dependence reported in Palandri and Kharaka, 2004, the dissolution
789 rate of orthoclase is 2.2×10^{-9} mol.m^{-2}.s^{-1} at pH 5.3 and 180 °C. For direct comparison with
790 previous simulations, porosity and coating thickness were maintained at 22% and 5.2 µm. The
791 results showed that at steady-state, the H^+ concentration in the cell contacting orthoclase is
792 $0.70C_0 = 3.5 \times 10^{-6}$ mol.L^{-1}, corresponding to an apparent dissolution rate of 1.9×10^{-9} mol.m^{-2}.s^{-1} (Fig. S11). The decrease in orthoclase dissolution rate thus reaches 15%, pointing out
794 that under such conditions, the secondary coating do not play a major role in orthoclase
795 dissolution kinetics. As a matter of fact, the observed drop in reactivity is close to that
796 calculated at pH 2. As a consequence, the gradual increase in pH after an acid stimulation will
797 not drastically modify the intrinsic impact of the coatings on orthoclase reactivity.

798 *4.4.3.2 Influence of coating thickness*

799 In order to estimate the impact of secondary coatings at further progress of reaction,
800 supplementary simulations were conducted, using a fixed porosity maintained at 22%,
801 corresponding to $D = 1.6 \times 10^{-9}$ m^2.s^{-1}. The results are reported in Fig. 15. A dramatic drop in
802 H^+ concentration in the cell in contact with orthoclase can be observed when increasing the
803 coating thickness, which translates into an equivalent drop in the orthoclase dissolution rate
804 (Fig. 15b). For coating thickness exceeding 30 µm, the dissolution rate decreased by nearly
805 one order of magnitude, illustrating that the coating thickness is a crucial parameter in the

buildup of a diffusion boundary layer at the interface with the primary silicate. Of note, similar conclusions were reached in previous studies (e.g., Emmanuel, 2022). Therefore, it is likely that in geothermal systems similar to that of Soultz-sous-Forêts, the primary minerals will be gradually isolated from the fluid circulations within timescales of a few months, according to the combined results of our experimental and simulation observations.

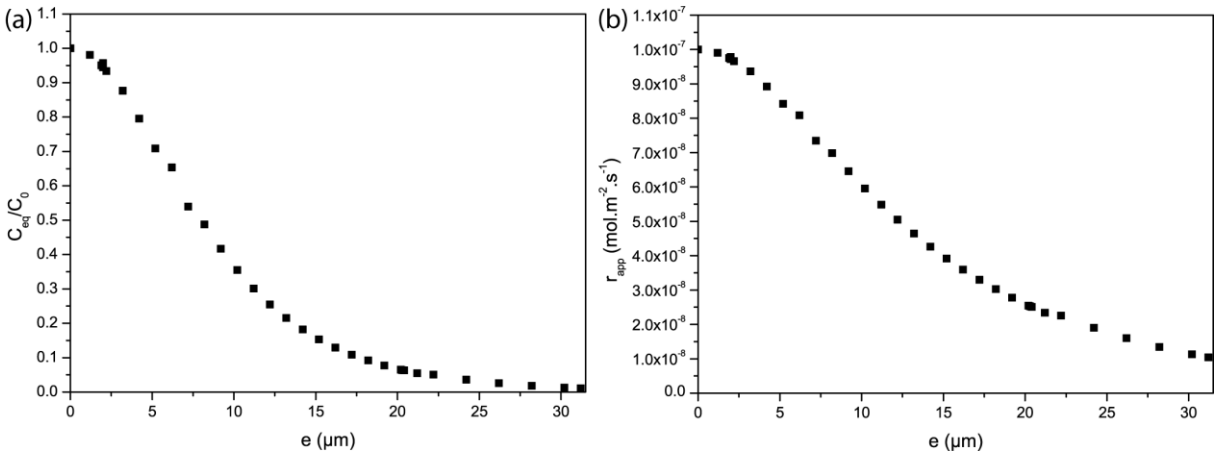

Fig. 15. Main results for the reactive transport simulations aimed at testing the impact of secondary coating thickness on orthoclase dissolution rate. (a) Evolution of the concentration of H^+ in the cell in contact with orthoclase with coating thickness. (b) Corresponding evolution of orthoclase dissolution rate. See text for details.

4.4.3.3 Influence of the intrinsic mineral dissolution rate

A striking feature of all previous simulations is that it was impossible to evidence a dramatic drop in the reactivity of the primary phase with coatings having thickness on the order of a few microns. However, Cubillas et al., 2005 observed a decrease of 1 to 2 orders of magnitude in the dissolution rate of calcite in the presence of secondary phase coatings with a thickness of between 3 and 10 µm. Their study was conducted with a mineral whose dissolution rate is much higher than that of orthoclase. In an attempt to explain these observations, the influence of the intrinsic dissolution rate constant is tested below.

To test whether the model developed here can reproduce such a drop in reactivity, simulations were carried out using a dissolution rate of 2.69×10^{-4} mol.m^{-2}.s^{-1}. This rate is of the same order of magnitude as that of calcite at pH 2 and 25 °C (Palandri and Kharaka, 2004;

828 Cubillas et al., 2005). It should also be noted that the dissolution rate of calcite varies
829 proportionally to the H^+ concentration (Palandri and Kharaka, 2004), as opposed to
830 orthoclase, whose dissolution rate varies proportionally to the square root of [H^+]. Therefore,
831 the sink term was adjusted to $P = \frac{2r_0}{\varphi_N \Delta x}\frac{C_N^t}{C_0}$.

832 Figure 16 shows the concentration profiles obtained with this dissolution rate. The
833 simulations were carried out for a coating with a porosity of 22% and a thickness of 5.2 µm or
834 10 µm. It can be seen that the steady-state concentration in the mesh in contact with the
835 dissolving mineral is much lower for calcite than for orthoclase (Fig. 16a-b), which translated
836 into an apparent dissolution rate of calcite of 1.30×10^{-4} mol.m^{-2}.s^{-1}. The observed reduction
837 in reactivity is 52% for calcite, whereas it was only around 16% for orthoclase (see section
838 *4.4.3*), illustrating the critical importance of the magnitude of the sink term in the steady-state
839 gradient of H^+ across the coating. The impact is even more dramatic if the thickness of the
840 coating is increased to 10 µm coating (Fig. 16c-d): Under these conditions, the apparent
841 dissolution rate of calcite is 5.75×10^{-5} mol.m^{-2}.s^{-1}, corresponding to a drop in reactivity of
842 80%. These results show that a coating of around ten µm on the calcite surface causes a drop
843 in reactivity of almost an order of magnitude. This is due to the very high rate at which H^+
844 ions are consumed by this mineral compared with their transport across the coating. Thus, the
845 observations of Cubillas et al., 2005 could, in part, be explained by this model.

846 *4.4.3.4 Concluding remarks and role of coatings on long-term scenarios*

847 The simple reactive transport model used here highlighted that the thickness of the
848 coatings and the intrinsic dissolution rate constant of the dissolving phases are the most
849 sensitive parameters that can eventually result in a decrease in the dissolution rate of the
850 primary minerals. Considering coatings of a few tens of µm and a high H^+ ion consumption
851 rate at the mineral surface (~ 10^6 times greater in the case of calcite than orthoclase), the drop
852 in reactivity induced by the limitation of H^+ ion transport within the coating can be significant

(approximately one order of magnitude). This explains why the presence of micron-thick coatings can have significant effects on calcite (Cubillas et al., 2005) and negligible effects on feldspars (Hellmann et al., 1989, this study).

Regarding the specific case of mineral reactivity in the granitic reservoir of Soultz-sous-Forêts, combining the experimental observations with modeling results lead to two main conclusions:

(i) first, in case of an acid stimulation aimed at removing barite scaling from the fractures, the exposure of fresh K-feldspar surfaces resulting from fluid circulation and barite removal will lead to the formation of new Al-rich coatings that will negligibly impact K-feldspar dissolution rates, as long those coatings do not fully cover the K-feldspar surfaces, and their thickness remains limited to a $\leq$ 10 µm.

(ii) Since K-feldspar is the main supplier of Ba (e.g., Azaroual and Fouillac, 1997), the exposure of K-feldspar surfaces will result in a sustained flux of Ba, which might ultimately limit the benefits of the acid stimulation. However, the outputs of the model also suggested that as soon as the Al-rich secondary coatings reach a thickness of several 10s of µm (which is expected to happen within a few months), then K-feldspar dissolution rate drops. Therefore, the increase in Ba release following enhanced K-feldspar dissolution should be transient only, and the benefit from acidic stimulation should be long-lasting.

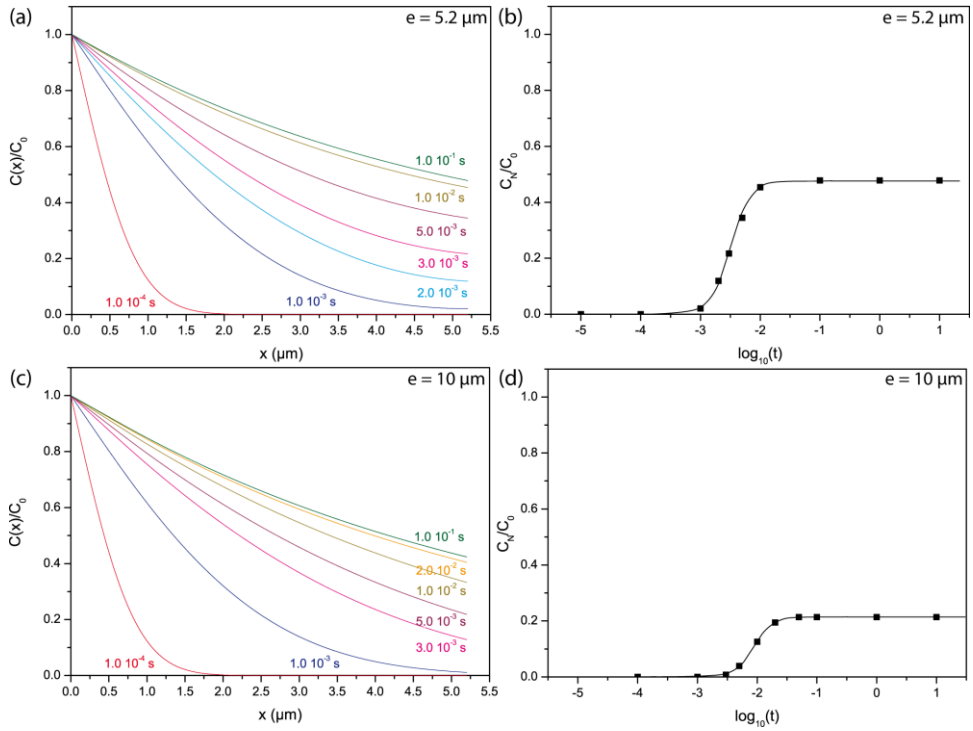

Fig. 16. Main results for the reactive transport simulations aimed at testing the impact of secondary coating on calcite dissolution rate at pH = 2 and 25 °C for a coating thickness of 5.2 µm (a, b) or 10 µm (c, d). The H^+ concentration across the coating as a function of time is represented in Figs 16a and 16c, while the concentration of H^+ in the mesh contacting calcite is represented in Figs. 16b and 16d. See text for details.

5. Conclusions

In this study, dissolution experiments and coupled dissolution-precipitation experiments were conducted to evaluate the impact of secondary coatings on the reactivity of orthoclase, a feldspar representing one of the main rock-forming minerals of the granitic reservoir of the Soultz-sous-Forêts geothermal system. This study was conducted in view of the limited existing literature aimed at quantifying the impact of secondary coatings on primary mineral dissolution at high pressure-high temperature conditions. Overall, we found that experiments conducted in conditions of supersaturation with respect to Al-bearing secondary phases resulted in a modest decline of orthoclase dissolution rate only. The precipitation of boehmite directly on orthoclase grains did not seem to significantly impact orthoclase reactivity, whose rate decrease may be better explained by the impact of dissolved Al in the bulk fluid. This

result was independently confirmed by running reactive transport simulations, which revealed that the impact of secondary coatings may become significant only when their thickness exceeds a few tens of microns, or if the reactivity of the primary phase is significantly greater (10^6 times) than that of orthoclase.

This study should be seen as a first step in a general effort aimed at better constraining the evolution of the 'effective surface area' of dissolving phases, a critical parameter for predicting mineral dissolution rates in the field, which is more often than not used as a fitting parameter in modeling exercises. Future studies may include experiments run over longer durations to enlighten the impact of the increase in coating thickness (suggested numerically to play an important role in the decrease in dissolution rate of the primary phases) and/or a change in the mineralogy of secondary phases, as clays might have an even more important armoring impact on silicate dissolution rates (e.g., Zhu, 2005).

Appendix

A1. Integration of the transport equation

The integral of the transport equation (Eq. 2) is defined as follows:

$$\int_{k-1/2}^{k+1/2} \varphi \frac{\partial C}{\partial t} dx = \int_{k-1/2}^{k+1/2} \frac{\partial}{\partial x}\left(D\left(\frac{\partial C}{\partial x}\right)\right) dx \quad \text{(A1)}$$

Using an implicit time scheme (discretization at t+1) the integrals for cell k can be expressed as:

$$E(k)C_k^{t+1} + F(k)C_{k+1}^{t+1} + G(k)C_{k-1}^{t+1} = C_k^t \quad \text{(A2)}$$

where:

$$E(k) = 1 + \frac{\Delta t}{\varphi_k \Delta x^2} D_{k+\frac{1}{2}} + \frac{\Delta t}{\varphi_k \Delta x^2} D_{k-\frac{1}{2}} \quad \text{(A3)}$$

$$F(k) = -\frac{\Delta t}{\varphi_k \Delta x^2} D_{k+\frac{1}{2}} \quad \text{(A4)}$$

914 $$G(k) = -\frac{\Delta t}{\varphi_k \Delta x^2} D_{k-\frac{1}{2}} \quad \text{(A5)}$$

915 Implementing the upstream and downstream boundary conditions, Equation (A1) can then be

916 written in matrix form as follows:

917 $$\begin{pmatrix} E(1) & F(1) & 0 & \dots & 0 & 0 & 0 \\ G(2) & E(2) & F(2) & \dots & 0 & 0 & 0 \\ 0 & \vdots & \vdots & \cdots & \vdots & 0 & 0 \\ 0 & \vdots & \vdots & \ddots & \vdots & \vdots & 0 \\ 0 & 0 & \vdots & \cdots & \vdots & \vdots & 0 \\ 0 & 0 & 0 & \dots & G(N-1) & E(N-1) & F(N-1) \\ 0 & 0 & 0 & \dots & 0 & G(N) & E(N) \end{pmatrix} \begin{pmatrix} C_1^{t+1} \\ C_2^{t+1} \\ \vdots \\ \vdots \\ \vdots \\ C_{N-1}^{t+1} \\ C_N^{t+1} \end{pmatrix} =$$

918 $$\begin{pmatrix} C_1^t - G(1)C_0 \\ C_2^t \\ \vdots \\ \vdots \\ \vdots \\ C_{N-1}^t \\ C_N^t - \frac{4r_0 \Delta t}{\varphi_N \Delta x} \sqrt{\frac{C_N^t}{C_0}} \end{pmatrix} \quad \text{(A6)}$$

919 where:

920 $$E(1) = 1 + \frac{\Delta t}{\varphi_1 \Delta x^2} D_{1+1/2} + \frac{2\Delta t}{\varphi_1 \Delta x^2} D_{1-\frac{1}{2}}$$

921 $$E(k) = 1 + \frac{\Delta t}{\varphi_k \Delta x^2} D_{k+\frac{1}{2}} + \frac{\Delta t}{\varphi_k \Delta x^2} D_{k-\frac{1}{2}}$$, for 1<k<N

922 $$E(N) = 1 + \frac{\Delta t}{\varphi_N \Delta x^2} D_{N-\frac{1}{2}}$$

923 $$F(k) = -\frac{\Delta t}{\varphi_k \Delta x^2} D_{k+\frac{1}{2}}$$, for 1≤k≤N

924 $$G(1) = -\frac{2\Delta t}{\varphi_1 \Delta x^2} D_{1-\frac{1}{2}}$$

925 $$G(k) = -\frac{\Delta t}{\varphi_k \Delta x^2} D_{k-\frac{1}{2}}$$, for 1<k≤N

926 The system of equations was solved using Gauss's direct Pivot method. Simulations were

927 performed with a cell size Δx = 1 nm and a constant time step $\Delta t = 10^{-6}$ s.

928

Acknowledgements

This work has been funded through a grant attributed to D.D. for the project "Feldspar reactivity in the context of Soultz-sous-Forêts: From microstructural characterizations to numerical modeling" under the framework of the LABEX ANR-11-LABX-0050_G-EAU-THERMIE-PROFONDE which benefits from a funding from the state managed by the French National Research Agency as part of the French ''Investissements d'avenir". M.P.-V. thanks the Région Alsace and LABEX ''G-EAU-THERMIE PROFONDE" for funding her PhD contract. Thanks are due to R. Boutin, G. Morvan and A. Aubert for their help with analyses and technical contributions at the LHyGeS (Strasbourg, France). Finally, critical inputs from 3 anonymous reviewers were much appreciated, and helped improve an earlier version of the manuscript.

References

Abràmoff, M.D., Magalhães, P.J., Ram, S.J., 2004. Image processing with ImageJ. Biophotonics international 11, 36-42.

Alt-Epping, P., Diamond, L.W., Häring, M., Ladner, F., Meier, D., 2013a. Prediction of water–rock interaction and porosity evolution in a granitoid-hosted enhanced geothermal system, using constraints from the 5 km Basel-1 well. Appl Geochem 38, 121-133.

Alt-Epping, P., Waber, H., Diamond, L.W., Eichinger, L., 2013b. Reactive transport modeling of the geothermal system at Bad Blumau, Austria: implications of the combined extraction of heat and CO2. Geothermics 45, 18-30.

Aradóttir, E., Sonnenthal, E., Björnsson, G., Jónsson, H., 2012. Multidimensional reactive transport modeling of CO 2 mineral sequestration in basalts at the Hellisheidi geothermal field, Iceland. Int J Greenh Gas Con 9, 24-40.

Archie, G.E., 1942. The electrical resistivity log as an aid in determining some reservoir characteristics. Transactions of the AIME 146, 54-62.

Azaroual, M., Fouillac, C., 1997. Experimental study and modelling of granite-distilled water interactions at 180 C and 14 bars. Appl Geochem 12, 55-73.

Burch, T.E., Nagy, K.L., Lasaga, A.C., 1993. Free energydependence of albite dissolution kinetics at 80°C and pH 8.8. Chem Geol 105, 137-162.

Cailleteau, C., Angeli, F., Devreux, F., Gin, S., Jestin, J., Jollivet, P., Spalla, O., 2008. Insight into silicate-glass corrosion mechanisms. Nature Materials 7, 978-983.

Cubillas, P., Kohler, S., Prieto, M., Causserand, C., Oelkers, E.H., 2005. How do mineral coatings affect dissolution rates? An experimental study of coupled CaCO3 dissolution-CdCO3 precipitation. Geochim Cosmochim Ac 69, 5459-5476.

Cui, G., Yang, L., Fang, J., Qiu, Z., Wang, Y., Ren, S., 2021. Geochemical reactions and their influence on petrophysical properties of ultra-low permeability oil reservoirs during water and CO2 flooding. Journal of Petroleum Science and Engineering 203, 108672.

Cui, G., Zhu, L., Zhou, Q., Ren, S., Wang, J., 2021. Geochemical reactions and their effect on CO2 storage efficiency during the whole process of CO2 EOR and subsequent storage. Int J Greenh Gas Con 108, 103335.

Daval, D., Bernard, S., Rémusat, L., Wild, B., Guyot, F., Micha, J.S., Rieutord, F., Magnin, V., Fernandez-Martinez, A., 2017. Dynamics of altered surface layer formation on dissolving silicates. Geochim Cosmochim Ac 209, 51-69.

Daval, D., Calvaruso, C., Guyot, F., Turpault, M.-P., 2018. Time-dependent feldspar dissolution rates resulting from surface passivation: Experimental evidence and geochemical implications. Earth Planet Sc Lett 498, 226-236.

Daval, D., Hellmann, R., Corvisier, J., Tisserand, D., Martinez, I., Guyot, F., 2010. Dissolution kinetics of diopside as a function of solution saturation state: Macroscopic measurements and implications for modeling of geological storage of CO2. Geochim Cosmochim Ac 74, 2615-2633.

Daval, D., Martinez, I., Corvisier, J., Findling, N., Goffe, B., Guyot, F., 2009a. Carbonation of Ca-bearing silicates, the case of wollastonite: Experimental investigations and kinetic modeling. Chem Geol 265, 63-78.

Daval, D., Martinez, I., Guigner, J.M., Hellmann, R., Corvisier, J., Findling, N., Dominici, C., Goffe, B., Guyot, F., 2009b. Mechanism of wollastonite carbonation deduced from micro- to nanometer length scale observations. Am Mineral 94, 1707-1726.

Dhanaraj, G., Byrappa, K., Prasad, V., Dudley, M., 2010. Springer handbook of crystal growth. Springer.

Emmanuel, S., 2022. Modeling the effect of mineral armoring on the rates of coupled dissolution-precipitation reactions: Implications for chemical weathering. Chem Geol 601, 120868.

Fournier, M., Ducasse, T., Pérez, A., Barchouchi, A., Daval, D., Gin, S., 2019. Effect of pH on the stability of passivating gel layers formed on International Simple Glass. Journal of Nuclear Materials 524, 21-38.

Fritz, B., Jacquot, E., Jacquemont, B., Baldeyrou-Bailly, A., Rosener, M., Vidal, O., 2010. Geochemical modelling of fluid-rock interactions in the context of the Soultz-sous-Forets geothermal system. Cr Geosci 342, 653-667.

Frugier, P., Gin, S., Minet, Y., Chave, T., Bonin, B., Godon, N., Lartigue, J.E., Jollivet, P., Ayral, A., De Windt, L., Santarini, G., 2008. SON68 nuclear glass dissolution kinetics: Current state of knowledge and basis of the new GRAAL model. Journal of Nuclear Materials 380, 8-21.

Gautier, J.M., Oelkers, E.H., Schott, J., 1994. Experimental-study of k-feldspar dissolution rates as a function of chemical affinity at 150-degrees-c and pH 9. Geochim Cosmochim Ac 58, 4549-4560.

Genter, A., Evans, K., Cuenot, N., Fritsch, D., Sanjuan, B., 2010. Contribution of the exploration of deep crystalline fractured reservoir of Soultz to the knowledge of enhanced geothermal systems (EGS). Cr Geosci 342, 502-516.

Gérard, A., Menjoz, A., Schwoerer, P., 1984. L'anomalie thermique de Soultz-sous-Forêts. Geothermal Actual 3, 35-42.

Gin, S., Jollivet, P., Fournier, M., Angeli, F., Frugier, P., Charpentier, T., 2015. Origin and consequences of silicate glass passivation by surface layers. Nat Commun 6.

Gin, S., Ribet, I., Couillard, M., 2001. Role and properties of the gel formed during nuclear glass alteration: importance of gel formation conditions, International Topical Workshop on Glass in its Disposal Environment. Elsevier Science Bv, Brugge, Belgium, pp. 1-10.

Godinho, J.R.A., Stack, A.G., 2015. Growth Kinetics and Morphology of Barite Crystals Derived from Face-Specific Growth Rates. Crystal Growth & Design 15, 2064-2071.

Golubev, S.V., Pokrovsky, O.S., 2006. Experimental study of the effect of organic ligands on diopside dissolution kinetics. Chem Geol 235, 377-389.

Griffiths, L., Heap, M.J., Wang, F., Daval, D., Gilg, H.A., Baud, P., Schmittbuhl, J., Genter, A., 2016. Geothermal implications for fracture-filling hydrothermal precipitation. Geothermics 64, 235-245.

Hellmann, R., Crerar, D.A., Zhang, R.H., 1989. Albite Feldspar Hydrolysis to 300-Degrees-C. Solid State Ionics 32-3, 314-329.

Hellmann, R., Daval, D., Tisserand, D., 2010. The dependence of albite feldspar dissolution kinetics on fluid saturation state at acid and basic pH: Progress towards a universal relation. Cr Geosci 342, 676-684.

Hellmann, R., Dran, J.C., DellaMea, G., 1997. The albite-water system .3. Characterization of leached and hydrogen-enriched layers formed at 300 degrees C using MeV ion beam techniques. Geochim Cosmochim Ac 61, 1575-1594.

Hellmann, R., Tisserand, D., 2006. Dissolution kinetics as a function of the Gibbs free energy of reaction: An experimental study based on albite feldspar. Geochim Cosmochim Ac 70, 364-383.

Lucas, Y., Ngo, V.V., Clément, A., Fritz, B., Schäfer, G., 2020. Modelling acid stimulation in the enhanced geothermal system of Soultz-sous-Forêts (Alsace, France). Geothermics 85, 101772.

1029 Luce, R.W., Bartlett, R.W., Parks, G.A., 1972. Dissolution kinetics of magnesium silicates. Geochim
1030 Cosmochim Ac 36, 33-50.
1031 Luttge, A., 2006. Crystal dissolution kinetics and Gibbs free energy. Journal of Electron Spectroscopy
1032 and Related Phenomena 150, 248-259.
1033 Maher, K., Steefel, C.I., White, A.F., Stonestrom, D.A., 2009. The role of reaction affinity and
1034 secondary minerals in regulating chemical weathering rates at the Santa Cruz Soil
1035 Chronosequence, California. Geochim Cosmochim Ac 73, 2804-2831.
1036 Montes-H, G., Fritz, B., Clement, A., Michau, N., 2005. Modelling of geochemical reactions and
1037 experimental cation exchange in MX80 bentonite. Journal of Environmental Management 77, 35-
1038 46.
1039 Munck, F., Walgenwitz, F., Maget, P., Sauer, K., Tietze, R., 1979. Synthèse géothermique du Fossé
1040 rhénan Supérieur. Commission of the European Communities 20.
1041 Ngo, V.V., Lucas, Y., Clément, A., Fritz, B., 2016. Modeling the impact of temperature on the
1042 saturation state and behavior of minerals in the Soultz-sous-Forêts geothermal system.
1043 Geothermics 64, 196-208.
1044 Oelkers, E.H., 2001. General kinetic description of multioxide silicate mineral and glass dissolution.
1045 Geochim Cosmochim Ac 65, 3703-3719.
1046 Oelkers, E.H., Schott, J., Devidal, J.-L., 1994. The effect of aluminum, pH, and chemical affinity on
1047 the rates of aluminosilicate dissolution reactions. Geochim Cosmochim Ac 58, 2011-2024.
1048 Palandri, J.L., Kharaka, Y.K., 2004. A compilation of rate parameters of water-mineral interaction
1049 kinetics for application to geochemical modeling, in: U.S. Geological Survey, O.F.R. (Ed.), p. 70.
1050 Pauwels, H., Fouillac, C., Goff, F., Vuataz, F.-D., 1997. The isotopic and chemical composition of
1051 CO2-rich thermal waters in the Mont-Dore region (Massif-Central, France). Appl Geochem 12,
1052 411-427.
1053 Pollet-Villard, M., Daval, D., Ackerer, P., Saldi, G.D., Wild, B., Knauss, K.G., Fritz, B., 2016a. Does
1054 crystallographic anisotropy prevent the conventional treatment of aqueous mineral reactivity? A
1055 case study based on K-feldspar dissolution kinetics. Geochim Cosmochim Ac 190, 294-308.
1056 Pollet-Villard, M., Daval, D., Fritz, B., Knauss, K.G., Schäfer, G., Ackerer, P., 2016b. Influence of
1057 etch pit development on the surface area and dissolution kinetics of the orthoclase (001) surface.
1058 Chem Geol 447, 79-92.
1059 Putnis, A., 2002. Mineral replacement reactions: from macroscopic observations to microscopic
1060 mechanisms, 18th General Meeting of the International-Mineralogical-Association. Mineralogical
1061 Society, Edinburgh, Scotland, pp. 689-708.
1062 Putnis, A., 2009. Mineral Replacement Reactions. Rev Mineral Geochem 70, 87-124.
1063 Ruiz-Agudo, E., King, H.E., Patiño-López, L.D., Putnis, C.V., Geisler, T., Rodriguez-Navarro, C.,
1064 Putnis, A., 2016. Control of silicate weathering by interface-coupled dissolution-precipitation
1065 processes at the mineral-solution interface. Geology 44, 567-570.

Ruiz-Agudo, E., Putnis, C.V., Putnis, A., 2014. Coupled dissolution and precipitation at mineral–fluid interfaces. Chem Geol 383, 132-146.

Saldi, G.D., Daval, D., Guo, H., Guyot, F., Bernard, S., Le Guillou, C., Davis, J.A., Knauss, K.G., 2015. Mineralogical evolution of Fe–Si-rich layers at the olivine-water interface during carbonation reactions. Am Mineral 100, 2655-2669.

Saldi, G.D., Daval, D., Morvan, G., Knauss, K.G., 2013. The role of Fe and redox conditions in olivine carbonation rates: An experimental study of the rate limiting reactions at 90 and 150 °C in open and closed systems. Geochim Cosmochim Ac 118, 157-183.

Sanjuan, B., Millot, R., Dezayes, C., Brach, M., 2010. Main characteristics of the deep geothermal brine (5km) at Soultz-sous-Forêts (France) determined using geochemical and tracer test data. Cr Geosci 342, 546-559.

Schneider, C.A., Rasband, W.S., Eliceiri, K.W., 2012. NIH Image to ImageJ: 25 years of image analysis. Nature methods 9, 671-675.

Stockmann, G., Wolff-Boenisch, D., Gislason, S.R., Oelkers, E.H., 2008. Dissolution of diopside and basaltic glass: the effect of carbonate coating, 8th International Symposium on the Geochemistry of the Earths Surface (GES-8). Mineralogical Soc, London, England, pp. 135-139.

Stockmann, G.J., Wolff-Boenisch, D., Gislason, S.R., Oelkers, E.H., 2011. Do carbonate precipitates affect dissolution kinetics? 1: Basaltic glass. Chem Geol 284, 306-316.

Stockmann, G.J., Wolff-Boenisch, D., Gislason, S.R., Oelkers, E.H., 2013. Do carbonate precipitates affect dissolution kinetics?: 2: Diopside. Chem Geol 337–338, 56-66.

Taylor, A.S., Blum, J.D., Lasaga, A.C., 2000. The dependence of labradorite dissolution and Sr isotope release rates on solution saturation state. Geochim Cosmochim Ac 64, 2389-2400.

van der Lee, J., De Windt, L., 2002. CHESS Tutorial and Cookbook. Updated for version 3.0., Paris.

Velbel, M.A., 1993. Formation of protective surface layers during silicate-mineral weathering under well-leached, oxidizing conditions. Am Mineral 78, 405-414.

Vital, M., Daval, D., Morvan, G., Martinez, D.E., Heap, M.J., 2020. Barite Growth Rates as a Function of Crystallographic Orientation, Temperature, And Solution Saturation State. Crystal Growth & Design 20, 3663-3672.

Zhu, C., 2005. In situ feldspar dissolution rates in an aquifer. Geochim Cosmochim Ac 69, 1435-1453.